

# Two New Long-Period Giant Planets from the McDonald Observatory Planet Search and Two Stars with Long-Period Radial Velocity Signals Related to Stellar Activity Cycles

Michael Endl<sup>1</sup>, Erik J. Brugamyer, William D. Cochran, Phillip J. MacQueen, Paul Robertson<sup>2,3</sup>, Stefano Meschiari, Ivan Ramirez, Matthew Shetrone, Kevin Gullikson, Marshall C. Johnson,

*McDonald Observatory and Department of Astronomy, University of Texas at Austin, Austin, TX 78712, USA*

Robert Wittenmyer,

*School of Physics and Australian Centre for Astrobiology, UNSW Australia, Sydney 2052, Australia*

Jonathan Horner,

*Computational Engineering and Science Research Centre, University of Southern Queensland, Toowoomba, Queensland 4350*

*Australian Centre for Astrobiology, UNSW Australia, Sydney 2052, Australia*

David R. Ciardi,

*NASA Exoplanet Science Institute & Infrared Processing and Analysis Center, California Institute of Technology, USA*

Elliott Horch,

*Department of Physics, Southern Connecticut State University, 501 Crescent St., New Haven, CT 06515, USA*

Attila E. Simon,

*Physikalisches Institut, Center for Space and Habitability, University of Bern, CH-3012 Bern, Switzerland*

Steve B. Howell,

*NASA Ames Research Center, Moffett Field, CA 94035 USA*

Mark Everett,

*National Optical Astronomy Observatory, 950 North Cherry Avenue, Tucson, AZ 85719 USA*

Caroline Caldwell,

*Astrophysics Research Institute, Liverpool John Moores University, 146 Brownlow Hill, Liverpool, L3 5RF, UK*

and

Barbara G.<sup>1</sup>Castanheira

*McDonald Observatory, University of Texas at Austin, Austin, TX 78712, USA*

## 1. Introduction

“How common are Solar System analogs?” Until relatively recently, this fundamental question had little in the way of observational answers. Although the *Kepler* mission (Borucki et al. 2010) has provided first constraints on the answer to the related question of “how common are Earth analogs?”, until our instruments and techniques improve to the point that we are capable of detecting planets across a range of masses and orbits analogous to those of the planets in our Solar System, a definitive answer is currently beyond our reach. However, as a next step we might instead ask: “how common are Jupiter analogs?”, gas giant planets that have either not significantly migrated inward from the location of their formation beyond the ice-line in the protoplanetary disk, or migrated inwards very early, followed by an episode of outward migration (the “Grand Tack” model; Walsh et al. 2011). As the time baseline of radial velocity searches grows, we are becoming better equipped to answer this last question.

The radial velocity (RV) technique has been used to detect/discover  $\sim 600$  of the  $\sim 2000$  known, confirmed exoplanets. Since the technique is heavily biased towards massive planets in short-period orbits, the majority of these are gas giants in orbits of less than one Earth-year. Only about 25 RV detected planets can be considered “Jupiter analogs”, which we define as within a factor of a few Jupiter-masses and in orbits longer than 8 years (about 3000 days). Although the *Kepler* mission – utilizing the planet transit method – has delivered  $\sim 1000$  planets and nearly 5000 candidates, none of these can be classified as “long-period”, due to the limited time baseline of the mission data.

To answer the question of the uniqueness of our solar system, it is probably more important to find and characterize long-period Jovian planets than to find small-radius terrestrial planets. Other studies (Howard et al. 2012, Wittenmyer et al. 2011b, Fressin et al. 2013, Petigura et al. 2013) have shown that terrestrial-size planets are quite

common around other stars, but the data concerning Jupiter analogs are quite incomplete due to the need for a time baseline of over 10-15 years. A handful of RV surveys have “outgrown” this time baseline selection bias: the Lick Observatory planet search from 1987 to 2011 (Fischer, Marcy & Spronck 2014), our ongoing McDonald Observatory Planet Search, the Anglo-Australian Planet Search (e.g. Wittenmyer et al. 2014a), the Keck/HIRES RV survey (e.g. Howard et al. 2014) and the planet search programs at CORALIE (e.g. Marmier et al. 2013) and HARPS (e.g. Moutou et al. 2015). An example of a Jupiter-analog planet orbiting a Solar twin is presented in Bedell et al. (2015). While the *Kepler* mission has revolutionized exoplanetary science and provided a first estimate of the frequency of Earth-size planets in Earth-like orbits, long-term radial-velocity surveys complement these data with measurements of the frequency of Jupiter-like planets in Jupiter-like orbits. This in turn will reveal how common Solar System-like architectures are.

While the idea that Jupiter analogs are required to shield terrestrial planets from impacts has been conclusively dismantled (e.g. Horner & Jones 2008, 2012; Horner, Jones & Chambers 2010), the presence of Jupiter analogs might be critical for the delivery of water to planets that would otherwise have formed as dry, lifeless husks (Horner & Jones 2010, Raymond 2006). The early dynamical evolution of Jupiter and Saturn might also be responsible for a depletion of the inner planetesimal disk, and for the subsequent formation of small, low-mass terrestrial planets, instead of large, massive super-Earths (Batygin & Laughlin 2015). The search for Jupiter analogs thus provides a key datum for models of planetary formation and evolution – attempting to answer the question “how common are planetary systems like our own?”

The McDonald Observatory Planet Search (Cochran & Hatzes 1993) is a high precision RV survey of hundreds of FGKM stars, begun in 1987 using the 2.7 m Harlan J. Smith telescope. Since our migration to our current instrumental configuration in 1998 (“Phase III”, described in Hatzes et al. 2003), we achieve routine long-term Doppler velocity precision of  $\sim 4\text{--}8\text{ m s}^{-1}$ . With this precision and an observational time baseline approaching 17 years, we are now sensitive to Jovian analogs. In this paper, we

---

<sup>1</sup>e-mail: mike@astro.as.utexas.edu

<sup>2</sup>Center for Exoplanets and Habitable Worlds, Department of Astronomy and Astrophysics, The Pennsylvania State University

<sup>3</sup>NASA Sagan fellow

present two new long-period planetary companions (HD 95872b and  $\psi^1$  Dra Bb). We also report two cases (HD 10086 and  $\beta$  Virginis) of Keplerian-like signals that mimic a Jupiter-type planet but are probably the result of stellar activity akin to the 11-year Solar cycle.

## 2. Observations

Our radial velocity measurements were obtained using the 2.7 m Harlan J. Smith and 10 m Keck I telescopes. The specific instruments/observations are described below.

### 2.1. Harlan J. Smith Telescope Observations

For the 2.7 m Harlan J. Smith Telescope (HJST), we utilize the cross-dispersed Echelle Tull Coude spectrograph (Tull et al. 1994). Our configuration uses a 1.2 arcsec slit, an Echelle grating with 52.67 groove  $\text{mm}^{-1}$ , and a 2048 $\times$ 2048 Tektronix CCD with 24  $\mu\text{m}$  pixels, yielding a resolving power ( $R = \lambda/\Delta\lambda$ ) of  $R = 60,000$ . The wavelength coverage extends from 3,750  $\text{\AA}$  to 10,200  $\text{\AA}$ , and is complete from the blue end to 5,691  $\text{\AA}$ , after which there are increasingly large inter-order gaps.

### 2.2. Keck Telescope Observations

For HD 95872, we also obtained 10 precise RV measurements using Keck I and its HIRES spectrograph (Vogt et al. 1994), during three observing runs allocated to the NASA CoRoT key science project, during times when the CoRoT fields were unobservable.

The spectra for HD 95872 were taken with HIRES with a resolving power of  $R = 50,000$ , using an instrumental setup similar to the California Planet Search (e.g. Howard et al. 2010). Also for HIRES we used an iodine cell to monitor real time instrumental variations relevant to measuring precise radial velocities.

### 2.3. Data Reduction

The raw CCD data were reduced using a pipeline implemented in the Image Reduction and Analysis Facility (IRAF) using standard routines within the `echelle` package. The process includes overscan trimming, bad pixel processing,

bias frame subtraction, scattered light removal, flat field division, order extraction, and wavelength solution application using a Th-Ar calibration lamp spectrum. Most cosmic rays are successfully removed via IRAF's interpolation routines; however, particularly troublesome hits are removed by hand.

## 3. Analysis

### 3.1. Radial Velocity Measurements

Our radial velocity measurements were obtained using our standard iodine cell RV reduction pipeline `Austral` (Endl, Kürster, & Els 2000). Our approach follows the standard iodine cell data analysis methodology: the stellar RV is calculated by comparing all spectra of the target star, taken with the iodine cell, with a high signal-to-noise (S/N) stellar template spectrum free of iodine lines. During regular RV observations the temperature-controlled iodine cell is inserted in the light path and superimposes a dense reference spectrum onto the stellar spectrum. The iodine lines thus provide a simultaneous wavelength calibration and allow the reconstruction of the shape of the instrumental profile at the time of observation. The iodine cell at the Tull spectrograph has been in regular operation for more than two decades.

### 3.2. Stellar Activity Indicators

As a check against photospheric activity masquerading as planet-like Keplerian motion, we measure the Ca H and K Mount Wilson  $S_{HK}$  index (Soderblom, Duncan & Johnson 1991, Baliunas et al. 1995, Paulson et al. 2002) simultaneously with each RV data point. In addition, we have calculated the line bisector velocity spans (BVSs; e.g. Hatzes, Cochran & Johns-Krull 1997) of lines outside the region of iodine cell absorption. These time-series measurements are then checked for any possible correlation(s) with the RV measurements.

### 3.3. Stellar Characterization

We determined stellar atmospheric parameters for all four stars using a traditional absorption line curve-of-growth approach, following a procedure similar to that outlined in Brugamyer et al. (2011). The method utilizes an updated list of

suitable Fe and Ti lines, the local thermodynamic equilibrium (LTE) line analysis and spectral synthesis code MOOG<sup>1</sup>, and a grid of 1-D, plane-parallel ATLAS9 (Kurucz 1993) model atmospheres. We first manually measured the equivalent widths of 132 Fe I and 41 Ti I lines, along with 18 Fe II and 8 Ti II lines, in our template spectra (without the reference iodine cell in the light path). With these measurements in hand, the stellar effective temperature is constrained by assuming and enforcing excitation equilibrium – by varying the model atmosphere temperature until any trends in derived abundances with temperature are removed. Surface gravity is constrained by assuming and enforcing ionization equilibrium – by varying the model atmosphere gravity until the derived abundances of neutrals and ions agree. Microturbulent velocity is constrained by forcing the derived abundances for stronger lines to match those for weaker lines. For these processes, we used a weighted average of Fe (2x) and Ti (1x) when computing the relevant slopes/offsets (as there are approximately twice as many Fe than Ti lines). This process is repeated iteratively until all conditions are satisfied simultaneously with a self-consistent set of stellar parameters.

The results of our stellar characterization are summarized in Table 1. Spectral types, photometric data, and parallaxes are taken from the ASCC-2.5 catalog (Version 3; Kharchenko & Roeser 2009). We also include mass and age estimates from Yonsei-Yale model isochrones (Yi et al. 2001, Kim et al. 2002).

Using the stellar parameters  $T_{\text{eff}}$ ,  $\log g$ ,  $[\text{Fe}/\text{H}]$ , and their errors, we determined the masses and ages of our stars using the procedure outlined in Ramirez et al. (2014) (their Section 4.5). Briefly, the location of each star on stellar parameter space was compared to that of stellar interior and evolutionary model predictions. The Yonsei-Yale isochrone grid was used in our implementation. Each isochrone point was given a probability of representing an observation based on its distance from the measured stellar parameters and weighted by the observational errors. Then, mass and age probability distribution functions were computed by adding the probabilities of individual isochrone points binned in mass and age, re-

spectively. The peaks of these distributions were adopted as the most probable mass and age, while the  $1\sigma$ -like widths were used to estimate the errors.

Contrary to a more common practice, we did not use parallaxes in our mass and age determinations. This is because one of our stars, HD 95872, does not have a reliable measurement of trigonometric parallax; this star was not included in the *Hipparcos* catalog. To maintain consistency in our analysis, we employed the spectroscopic  $\log g$  values as luminosity indicators instead of absolute magnitudes computed using measured parallaxes. If we had used the *Hipparcos* parallaxes for the three stars which have those values available, their masses would be only about  $0.01 \pm 0.01 M_{\odot}$  smaller.

### 3.4. Planetary Orbit Modeling

We performed our planetary orbit modeling using the **Systemic Console**<sup>2</sup> package (Meschiari et al. 2009), a software application for the analysis and fitting of Doppler RV data sets.

## 4. The planet around HD 95872

The star HD 95872 was originally selected for RV monitoring from a sample of 22 thin disk stars observed on the 2.7 m HJST in 1998 for a project to characterize the metal rich end of chemical evolution of the Galactic disk. The sample of 22 stars were selected by M. Grenon (Observatoire de Geneve) for Sandra Castro (ESO) and Matthew Shetrone on the basis of their extreme kinematic (perigalactica  $\sim 3$  kpc) and photometric properties.

### 4.1. Keplerian solution

Table 2 presents the complete set of our RV measurements for HD 95872 from the HJST/Tull survey, as well as 10 additional measurements obtained with Keck/HIRES. The RV coverage spans approximately 11 years of monitoring over 44 measurements. The median internal uncertainty for our observations is  $\approx 6 \text{ m s}^{-1}$ , and the peak-to-peak velocity is  $\approx 137 \text{ m s}^{-1}$ . The velocity scatter around the average RV is  $\approx 32.1 \text{ m s}^{-1}$ .

<sup>1</sup>available at <http://www.as.utexas.edu/~chris/moog.html>

<sup>2</sup>available at <http://www.stefanom.org/systemic/>



TABLE 1  
STELLAR PROPERTIES

Star	Spectral Type	V	B-V	M <sub>V</sub>	Parallax (mas)	Dist. (pc)	T <sub>eff</sub> (K)	log g	[Fe/H]	Mass (M <sub>⊙</sub> )	Age (Gyr)
HD 95872	K0V	9.895	0.827	10.50	132.30	7.56	5312 ± 100	4.43 ± 0.15	0.41 ± 0.09	0.95 ± 0.04	10.0 ± 3.7
ψ <sup>1</sup> Dra B	G0V	5.699	0.562	3.97	45.13	22.16	6212 ± 75	4.20 ± 0.12	0.01 ± 0.06	1.19 ± 0.07	3.3 ± 1.0
HD 10086	G5IV	6.610	0.688	4.97	46.99	21.28	5722 ± 65	4.43 ± 0.10	0.10 ± 0.04	1.01 ± 0.03	5.5 ± 2.3
β Vir	F8V	3.589	0.568	3.40	91.65	10.91	6145 ± 75	3.98 ± 0.12	0.15 ± 0.05	1.34 ± 0.10	3.2 ± 0.7

	BJD	dRV (m s <sup>-1</sup> )	Uncertainty (m s <sup>-1</sup> )
1	2453073.8686	66.2	5.3
2	2453463.7752	98.5	5.9
3	2453843.7736	109.2	5.9
4	2454557.7575	63.5	6.7
5	2455286.7123	-22.2	4.1
6 <sup>a</sup>	2455366.7841	15.5	1.9
7 <sup>a</sup>	2455368.7876	13.3	3.5
8	...	...	...

Table 2: Differential radial velocity observations for HD 95872 (sample)

<sup>a</sup>Observed with Keck/HIRES; all others with the HJST/Tull.

The second panel shows the error-weighted, normalized Lomb-Scargle periodogram (Zechmeister & Kürster 2009). The three horizontal lines in the plot represent different levels of false alarm probability (FAP; 10%, 1% and 0.1%, respectively). The FAPs were computed by scrambling the data set 100,000 times, in order to determine the probability that the power at each frequency could be exceeded by chance (e.g. Kürster et al. 1997, Marcy et al. 2005). Computing the FAPs for this sparse data set required scanning only frequencies that were effectively sampled by the set of observation times. We determined an “effective” Nyquist frequency for the data set using the calculation formula of Koen (2006). For irregularly spaced data sets, the effective Nyquist frequency is much higher than the corresponding Nyquist frequency of a regularly spaced data set of the same size. The algorithm of Koen (2006) finds a clear minimum at  $P \approx 2$  days (bottom panel of Figure 1), corresponding to the effective Nyquist frequency for the data. Accordingly, we exclude periods shorter than 2 days from our calculations.

Visual inspection of the 44 individual RV measurements suggests the presence of a sparsely sampled, long-period signal (see top panel of Figure 2). The Lomb-Scargle periodogram (Figure 1) bears this out. The two strongest signals, at  $P = 29.6$  days ( $\text{FAP} < 4.0 \times 10^{-5}$ ) and  $P = 331.2$  days ( $\text{FAP} = 1.1 \times 10^{-2}$ ) have significant power in the window function, and they are likely related to the periodicities in the observational cadence (the lunar synodic month and the Solar year). The remaining peak is at  $P = 3922.05$  days ( $\text{FAP} = 2 \times 10^{-4}$ ). This signal is well fit with a Keplerian orbit of period  $P = 4278 \pm 169$  days and semi-amplitude  $K = 59 \pm 4$  m s<sup>-1</sup> (Figure 2). Together with the assumed stellar mass of  $0.95 M_{\odot}$ , this implies a minimum mass of  $M \sin i = 4.6 \pm 0.3 M_J$  and a semi-major axis  $a = 5.2 \pm 0.13$  AU. The best-fit orbit for the planet shows a small amount of eccentricity ( $e = 0.06 \pm 0.04$ , broadly consistent with circular). Orbital uncertainties were derived by running a Markov Chain Monte Carlo (MCMC) algorithm (Ford 2005, 2006, Meschiari et al. 2009, Gregory 2011) on the data set. Non-informative priors were adopted over all parameters (uniform in logarithm for mass and period). Marginal distributions of the parameters are shown in Figure 3; no significant correlations among parameters were observed. A summary of the astrometric orbital elements of HD 95872b is reported in Table 3.

The one-planet fit reduces the root mean square (RMS) of the data from 46.8 m s<sup>-1</sup> to 8.1 m s<sup>-1</sup>. The stellar jitter for HD 95872 (that is, the amount of noise added in quadrature to the formal uncertainties required in order to completely fit the residuals) is  $8 \pm 2$  m s<sup>-1</sup>, and is derived self-consistently from the MCMC analysis. We note that the normalized residuals are very nearly normally distributed, aside from a single outlier (Figure 4).

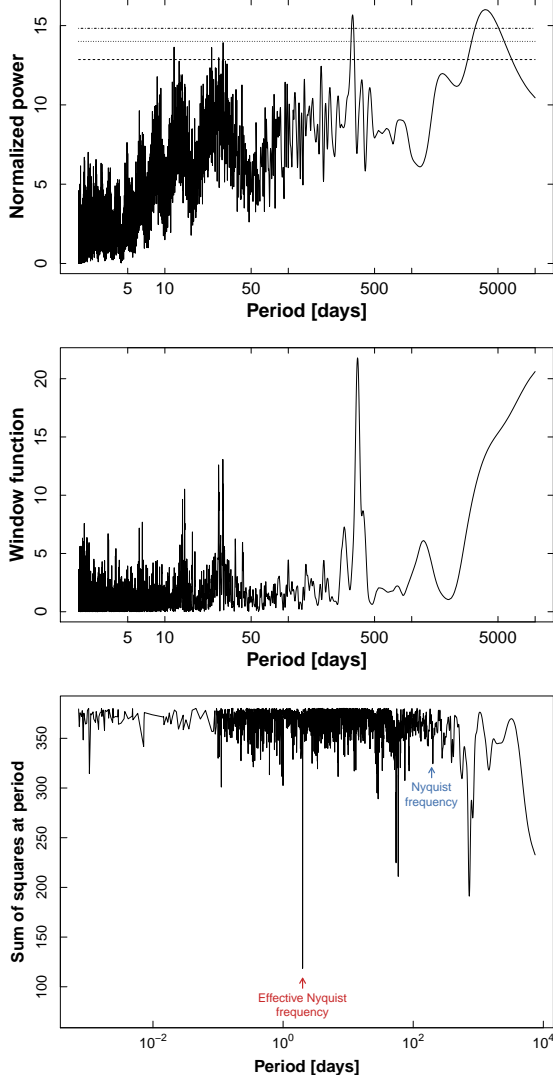


Fig. 1.— *Top panel:* Generalized Lomb-Scargle periodogram for the HD 95872 RV data. False-alarm probability levels are shown at the 10%, 1% and 0.1% level. *Middle panel:* Periodogram of the window function. *Bottom panel:* Determination of the “effective” Nyquist frequency for the data set. Both the effective Nyquist frequency, and the corresponding Nyquist frequency for a regularly spaced data set are marked.

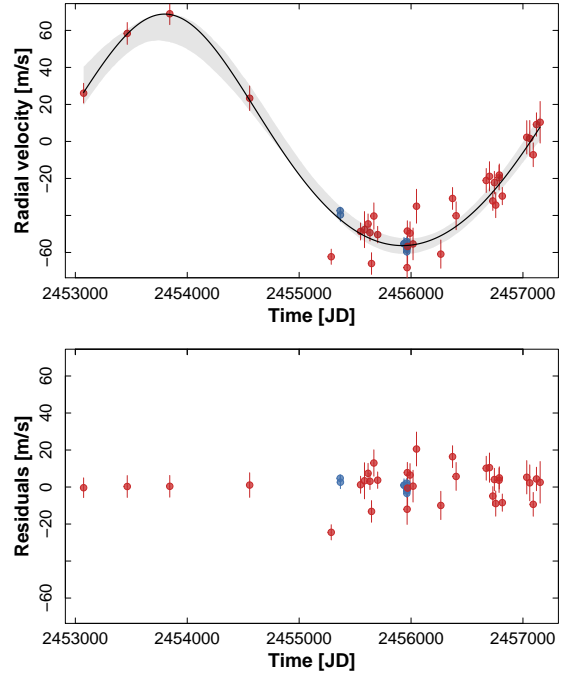


Fig. 2.— *Top panel:* Our RV data from HJST/Tull (red) and Keck/HIRES (blue) and the best-fit Keplerian model. The shaded area marks the 10%-90% percentiles of the radial velocity curves sampled from the MCMC trials, and indicates the range of the models compatible with the data. *Bottom panel:* Radial velocity residuals.

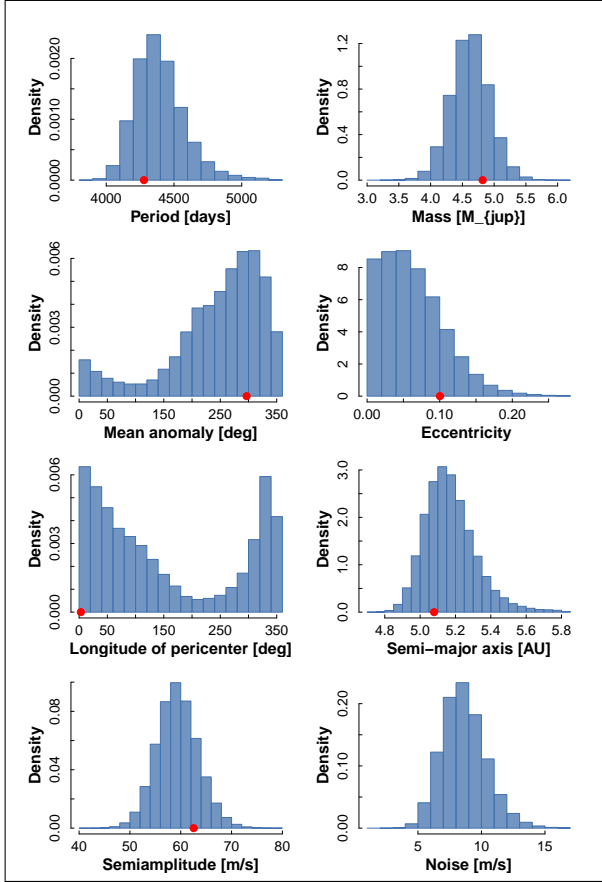


Fig. 3.— Marginal distributions of the orbital elements of HD 95872b, as computed by the Markov-Chain Monte Carlo algorithm. The red dot marks the value of the best-fit solution.

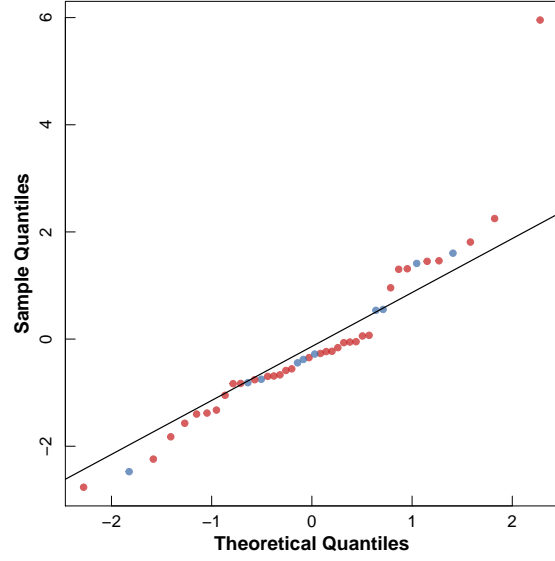


Fig. 4.— Quantile-quantile plot of the residuals from the 1-planet model for HD 95872. Perfectly normally distributed residuals would fall on the solid line.

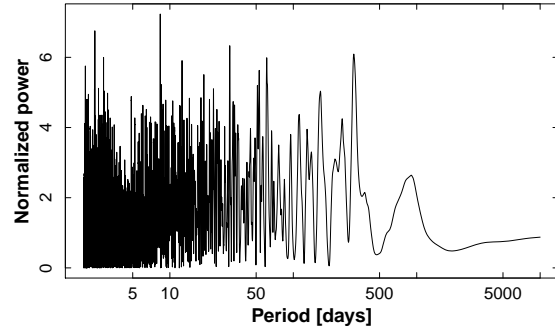


Fig. 5.— Lomb-Scargle periodogram of the residuals. All peaks have a FAP  $\leq 10\%$ .

Figure 5 shows the Lomb-Scargle periodogram of the RV residuals from the 1-planet best fit. There is no strong periodicity (FAP < 10%) in the residuals supporting the presence of additional planets in the system.

	HD 95872b
Period [days]	4375 [169]
Mass [ $M_{jup}$ ]	4.6 [0.3]
Mean anomaly [deg]	283 [65]
Eccentricity	0.06 [0.04]
Longitude of pericenter [deg]	17 [67]
Semi-amplitude [m/s]	59 [4]
Semi-major axis [AU]	5.2 [0.1]
Periastron passage time [JD]	2449869 [744]
Noise parameter, KECK data [m/s]	0.5 [0.6]
Noise parameter, McDonald data [m/s]	8 [2]
RV offset Keck/McDonald [m/s]	19 [2]
Stellar mass [ $M_{sun}$ ]	0.95
RMS [m/s]	7.90
Jitter (best fit) [m/s]	4.80
Epoch [JD]	2453073.87
Data points	44
Span of observations [JD]	2453073.87 (Asp 2004b) 2457153.62 (Mey 2003)

Table 3: Orbital elements for HD 95872b. For parameters derived from the MCMC analysis, we report their median values and their mean absolute deviation (in brackets).

#### 4.2. Stellar Activity Check

The large amplitude of  $\sim \pm 60 \text{ m s}^{-1}$  of the detected RV signal makes it unlikely that a long-term magnetic cycle is responsible for it. The relative faintness of this star ( $V = 9.9$ ) leads to very low S/N values in the blue spectral orders that contain the Ca II H & K lines at 390 nm. Therefore, we cannot determine a reliable time series of  $S_{HK}$  index measurements for this star using the Tull spectra. However, 9 HIRES spectra have sufficient S/N to obtain the  $S_{HK}$  index value. We calculate the  $R'_{HK}$  value following Paulson et al. (2002). We find  $R'_{HK} = -5.46 \pm 0.044$  for HD 95872. This means that HD 95872 is an inactive star and that the planetary hypothesis for the detected RV variation is the preferred one. Figure 6 shows the Ca II H & K lines from the HIRES spectrum with the highest S/N. There is nearly no chromospheric

emission detectable in the line cores, in agreement with the very low value of  $R'_{HK}$ .

Stellar activity can also manifest itself as variation of the average line shape. We therefore measured the velocity span of the line bisector (BVS) in the iodine-free regions of our Tull spectra. We find a mean BVS value of  $-0.05 \text{ km s}^{-1}$  with an rms-scatter of  $0.077 \text{ km s}^{-1}$ . The average  $1\sigma$  error on the BVS results is  $0.052 \text{ km s}^{-1}$ . We do not find any gross variability in the line bisectors that would cast doubt on the planetary origin of the signal. The average uncertainty of the BVS measurements is comparable to the detected RV signal which limits the usefulness of this analysis. The large uncertainty of  $\sim 50 \text{ m s}^{-1}$  is – again – due to the low S/N of spectra of this relative faint target star.

### 5. The $\psi^1$ Draconis System

The  $\psi^1$  Draconis system is a visual binary composed of an F5 V primary ( $\psi^1$  Dra A, 31 Dra A, HR 6636, HD 162003, HIP 86614) and an F8 V secondary star ( $\psi^1$  Dra B, 31 Dra B, HR 6637, HD 206204, HIP 86620) separated by about 30.1 arcsec. At a distance of 22.2 pc, this corresponds to a sky-projected separation of approximately 667 AU. Previously, Toyota et al. (2009) reported evidence of an unseen companion orbiting the A component of the system, with a minimum mass of  $50 M_J$ . We have monitored both stars for long-term RV variability and also find evidence for a stellar-mass companion around the A component. Moreover, we discovered two planetary/sub-stellar companions orbiting the B component. Thus, the  $\psi^1$  Draconis system is at least a hierarchical triple system, with the primary having a low-mass, K- or M-dwarf, companion and the secondary having two candidate planetary/sub-stellar companions.

#### 5.1. $\psi^1$ Draconis A

Table 4 presents the complete set of our RV observations for the primary star  $\psi^1$  Dra A. The RV coverage spans nearly 15 years of monitoring over 77 RV measurements. The median internal uncertainty for our RV data is  $\approx 15 \text{ m s}^{-1}$ , and the peak-to-peak velocity change is  $> 10,000 \text{ m s}^{-1}$ , typical for a stellar companion. The most recent RV measurements revealed that the star has passed the maximum of its RV orbit and is now

approaching a periastron passage (see Figure 7).

We performed a similar orbit fitting analysis as in the case of HD 95872. The marginal distributions of the orbital elements are shown in Figure 8. The binary orbit due to the stellar companion to  $\psi^1$  Dra A has a period of  $P \approx 6600$  d, an eccentricity of  $e \approx 0.67$  and a semi-amplitude of  $K \approx 5160$  m s $^{-1}$ . These values are consistent with a low mass stellar companion ( $\psi^1$  Dra C) to the primary at an orbital separation of  $a \approx 9$  AU. Table 5 summarizes the orbital elements that we determined from the RV data.

	BJD	dRV (m s $^{-1}$ )	Uncertainty (m s $^{-1}$ )
1	2451809.6596	1946.7	12.8
2	2451809.6740	1947.4	14.3
3	2452142.6805	1862.1	11.9
4	2453319.6392	2450.7	11.4
5	...	...	...

Table 4: Differential radial velocity measurements for  $\psi^1$  Draconis A (sample)

Parameter	Value [uncertainty]
Period [days]	6649 [160]
Mass [ $M_{jup}$ ]	551 [5]
Mean anomaly [deg]	70 [7]
Eccentricity	0.674 [0.004]
Long. of pericenter [deg]	32.9 [0.7]
Semi-amplitude [m/s]	5159 [27]
Semi-major axis [AU]	8.7 [0.1]
Periastron passage time [JD]	2450515 [162]
Noise parameter [m/s]	75 [6]
Stellar mass [ $M_{sun}$ ]	1.430
Chi-square	85.673
Log likelihood	486.353
RMS [m/s]	74.231
Jitter (best fit) [m/s]	72.617
Epoch [JD]	2451809.660
Data points	85
Span of observation [JD]	2451809.6596 (Sep. 2000) – 2457248.6070 (Aug. 2015)

Table 5: Orbital elements for the single-lined spectroscopic binary orbit of  $\psi^1$  Draconis A & C.

One striking feature of these orbital solutions are the large values of residual RV scatter around

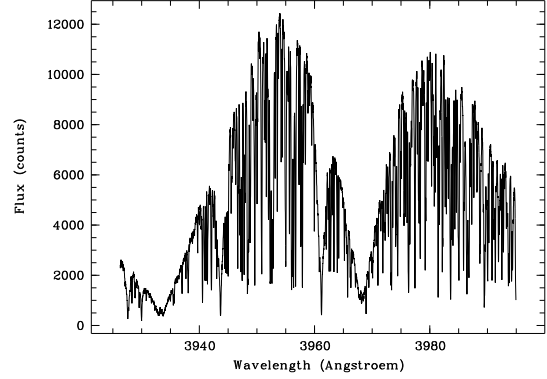


Fig. 6.— The Ca II H & K lines of HD 95872 in our best Keck/HIRES spectrum. The very low level of chromospheric emission in the line kernel shows that this star is quiet and inactive with  $R'_{HK} = -5.46 \pm 0.044$ .

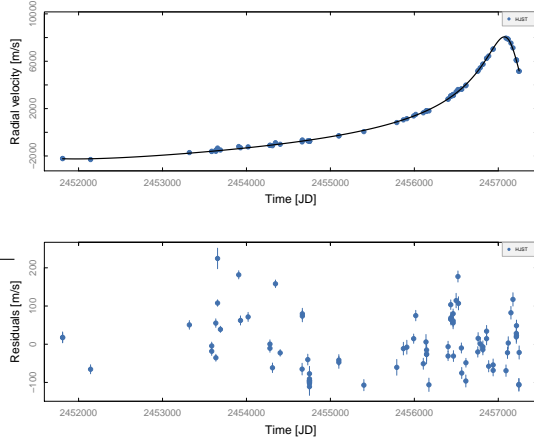


Fig. 7.— Top panel: our RV data for  $\psi^1$  Dra A showing an eccentric binary orbit with a period of  $P \approx 6650$  d (nearly 20 years). Bottom panel: RV residuals from the binary orbit. We find a large excess scatter of  $\approx 70$  m s $^{-1}$  indicating significant intrinsic stellar variability.

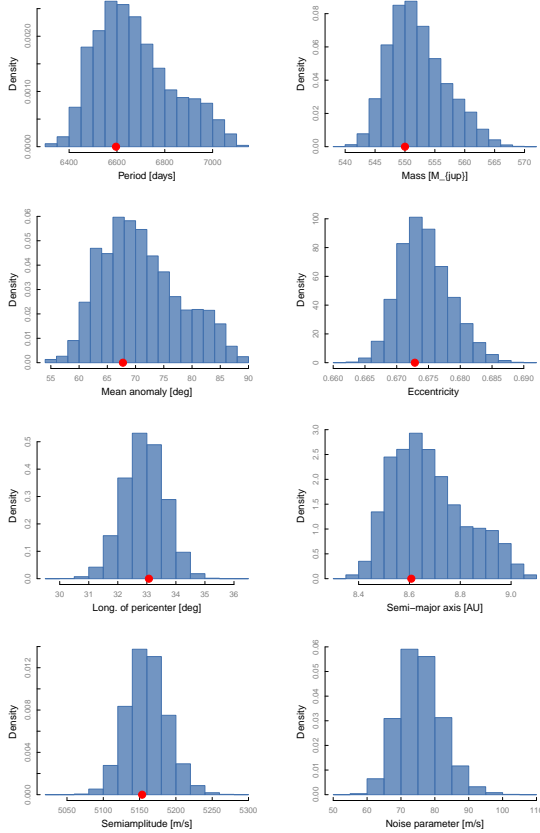


Fig. 8.— Marginal distributions of the orbital elements for the single-lined spectroscopic binary orbit of  $\psi^1$  Draconis A, as computed by the Markov-Chain Monte Carlo algorithm. The red dot marks the value of the best-fit solution.

the fit considering our typical RV uncertainties of  $\approx 15 \text{ m s}^{-1}$ . The models require an astrophysical noise term of  $\approx 75 \text{ m s}^{-1}$  to achieve a good fit. The Lomb-Scargle periodogram of the best-fit RV residuals (Figure 9) does not show any convincing periodic signals that could indicate additional companions in the system. However, with an F5V spectral type classification,  $\psi^1$  Dra A is one of earliest spectral types in our target list. In the HR-diagram this star is located close to the red edge of the instability strip. We therefore examined the *Hipparcos* photometry (ESA 1997) of  $\psi^1$  Dra A to search for stellar pulsations. The Fourier-transform of the photometry is displayed in Figure 10. We find a peak at a period of 2.1 hours ( $= 11.29$  cycles/day) with a modulation amplitude of  $> 4\sigma$ . This period value falls within the range of a few hours of typical p-mode oscillations of  $\delta$  Scuti-type pulsators (e.g. Balona, Daszyńska-Daszkiewicz & Pamyatnykh 2015). We therefore suspect that these stellar oscillations are responsible for the large observed excess scatter.

In section 5.3 we will discuss in more detail the detection of  $\psi^1$  Dra C, the stellar companion, by direct imaging. Owing to the small angular separation between  $\psi^1$  Dra A and C we expect that some of the residual scatter is also caused by contamination from light from the faint companion star that also entered through the spectrograph slit. In a companion paper (Gullikson et al. 2015) we successfully retrieve the Doppler signal of the low-level secondary spectrum and thus determine a double-lined spectroscopic orbital solution for  $\psi^1$  Dra A/C.

## 5.2. $\psi^1$ Draconis B

	BJD	dRV ( $\text{m s}^{-1}$ )	Uncertainty ( $\text{m s}^{-1}$ )	$S_{HK}$	Uncertainty
1	2451066.7344	-48.8	6.1	0.155	0.0198
2	2451121.6124	-48.5	3.8	0.161	0.0213
3	2451271.9939	-39.1	7.3	0.163	0.0197
4	2451329.8559	-33.4	5.5	0.162	0.0206
5	2451360.8829	-39.1	4.2	0.162	0.0214
6	2451417.7778	-24.5	5.0	0.173	0.0214
7	2451451.6921	-24.9	6.1	0.167	0.0217
8	...	...	...	...	...

Table 6: Differential radial velocity and Ca H&K observations for  $\psi^1$  Dra B (sample)

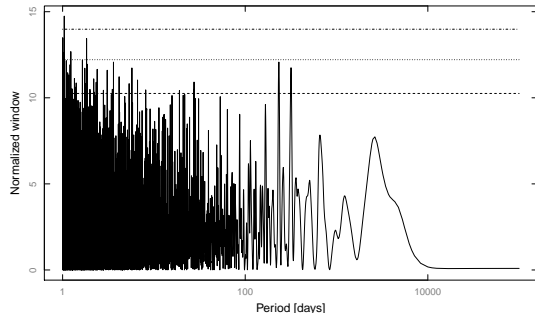


Fig. 9.— Generalized Lomb-Scargle periodogram of the best-fit RV residuals from the binary orbital solution. The horizontal dashed lines show FAP levels of 10%, 1% and 0.1% respectively.

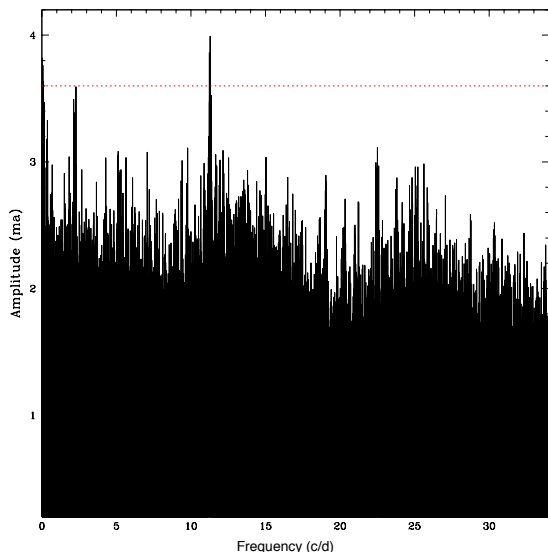


Fig. 10.— Fourier transform of the *Hipparcos* photometry of  $\psi^1$  Dra A revealing a strong peak at a frequency of 11.29 cycles/day ( $P = 2.1$  hours). The horizontal dashed line shows the  $4\sigma$ -level (FAP  $\approx 0.001$ ) of significance. The detected period of 2.1 hours is typical for non-radial stellar oscillations of a classic  $\delta$  Scuti variable.

Table 6 presents the complete set of our RV observations for  $\psi^1$  Dra B. The RV coverage spans approximately 16 years of monitoring over 135 measurements. The median internal uncertainty for our observations is  $\approx 5.6 \text{ m s}^{-1}$ , and the peak-to-peak velocity is  $\approx 62 \text{ m s}^{-1}$ . The velocity scatter around the average RV is  $\approx 14.3 \text{ m s}^{-1}$ .

### 5.2.1. Companion Orbit Models

The differential RV data for  $\psi^1$  Dra B are plotted in Figure 11. The Lomb-Scargle periodogram (Figure 11) for the RV data shows two strong peaks at  $P_1 \approx 2381$  days and  $P_2 > 6000$  days (longer than the time span of our observations). We model the second signal with two parameters representing a linear and a quadratic term (evaluated at the epoch of the fit).

Once the linear and quadratic trend terms are removed (Figure 12), a strong periodicity arises at  $P \approx 3030$  days. The bootstrapped FAP probability is very low ( $FAP < 2 \times 10^{-5}$ ). We fit this periodicity with a model that simultaneously minimizes the linear and quadratic trend terms and the five orbital elements describing an eccentric orbit (period, mass, mean anomaly, eccentricity and longitude of periastron). The best-fit model is shown in Figure 13. The data are well modeled by a Keplerian orbit of period  $P = 3117 \pm 42$  days and semi-amplitude  $K = 20.6 \pm 1.4 \text{ m s}^{-1}$ . Together with the assumed stellar mass of  $1.19 M_{\odot}$ , this implies a minimum mass of  $M \sin i = 1.53 \pm 0.09 M_J$  and a semi-major axis  $a = 4.43 \pm 0.04 \text{ AU}$ . No compelling peaks are evident in the periodogram of the residuals (bottom panel in Figure 13. Figure 14 displays the RV data phased to the orbital period of the planet.

The data strongly favor a substantial eccentricity for  $\psi^1$  Dra Bb ( $e = 0.40 \pm 0.05$ ). The cross-validation algorithm (Andrae et al. 2010) corroborates the clear preference for an eccentric model ( $\log \mathcal{L}_{circular} \approx 0.02$  vs.  $\log \mathcal{L}_{eccentric} \approx -21.3$ ; lower is better).

The distribution of the orbital elements is shown in Figure 15. There is no strong correlation between any of the parameters of the fit, including between the trend parameters and the semi-amplitude of the planet (bottom row). The derived stellar jitter is  $4.5 \pm 0.7 \text{ m s}^{-1}$ . The distribution of the residuals shows no evidence for

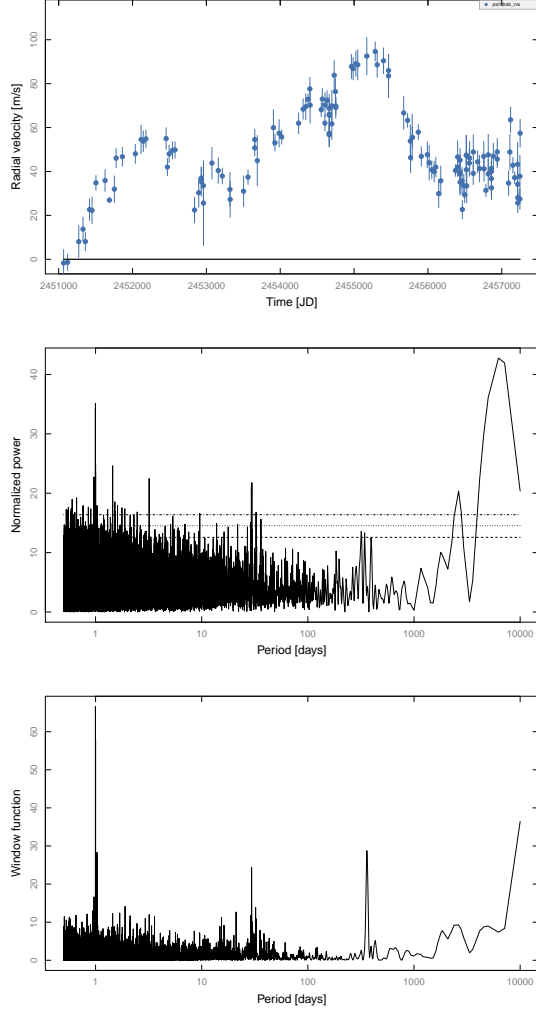


Fig. 11.— Radial velocity and Lomb-Scargle periodograms for  $\psi^1$  Dra B. *Top panel:* Our differential RV data. *Middle panel:* Error-weighted Lomb-Scargle periodogram for  $\psi^1$  Dra B. False-alarm probability levels are shown at the 10%, 1% and 0.1% level. *Bottom panel:* Periodogram of the window function.

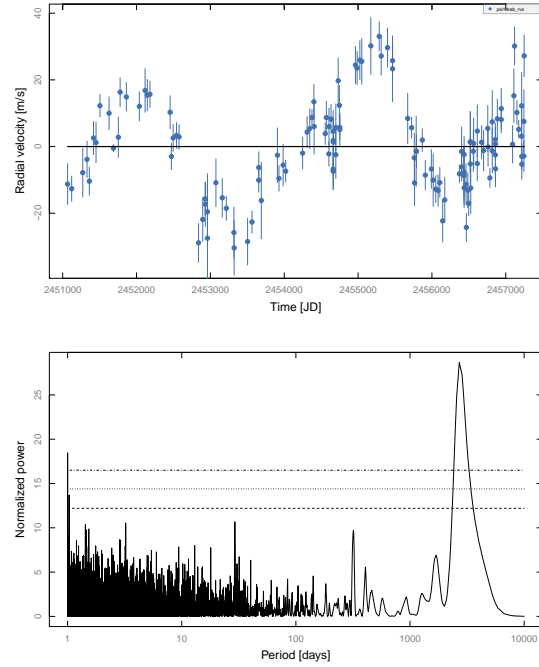


Fig. 12.— Radial velocity and Lomb-Scargle periodograms for  $\psi^1$  Dra B, with the linear and quadratic trends removed. *Top panel:* Relative RV data. *Bottom panel:* Error-weighted Lomb-Scargle periodogram for  $\psi^1$  Dra B. False-alarm probability levels are shown at the 10%, 1% and 0.1% level.



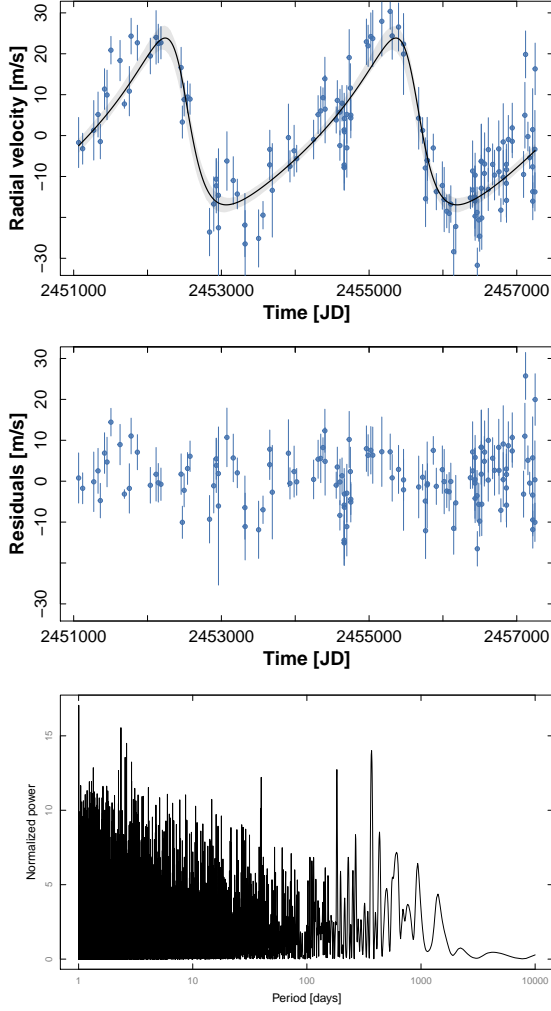


Fig. 13.— Best 1-planet fit of the RV data set for  $\psi^1$  Dra B. *Top*: Radial velocity observations (linear and quadratic term subtracted) and 1-planet best fit. The shaded area marks the 10%-90% percentiles of the radial velocity curves sampled from the MCMC trials, and indicates the range of the models compatible with the data. *Middle*: Residuals from the 1-planet best fit. *Bottom*: Periodogram of the residuals from the 1-planet best fit.

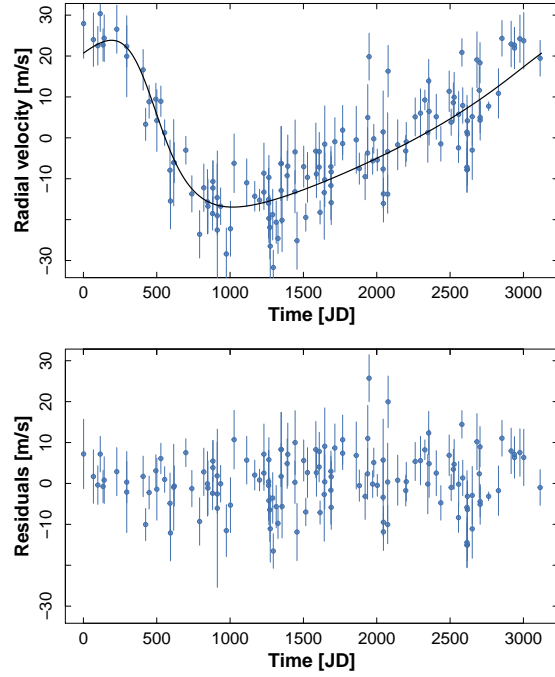


Fig. 14.— Phased best 1-planet fit of the RV data set for  $\psi^1$  Dra B. *Top*: Radial velocity observations (linear and quadratic term subtracted) and 1-planet best fit. *Bottom*: Residuals from the 1-planet best fit.

unmodeled periodicities in the data. Indeed, we note that the normalized residuals are again very nearly normally distributed (Figure 16).

$\psi^1$ Dra Bb	
Period [days]	3117 [42]
Mass [ $M_{jup}$ ]	1.53 [0.10]
Mean anomaly [deg]	199 [7]
Eccentricity	0.40 [0.05]
Long. of pericenter [deg]	64 [9]
Semi-amplitude [m/s]	21 [1]
Semi-major axis [AU]	4.43 [0.04]
Periastron passage time [JD]	2449344 [76]
Noise parameter [m/s]	4.5 [0.7]
Quadratic trend [m/s <sup>2</sup> ]	-0.0000041 [0.0000002]
Linear trend [m/s]	0.032 [0.002]
Stellar mass [ $M_{sun}$ ]	1.19
RMS [m/s]	7.048
Jitter (best fit) [m/s]	3.250
Epoch [JD]	2451066.734
Data points	135
Span of observations [JD]	2451066.7344 (Oct. 1998)
	2457248.6109 (Aug. 2015)

Table 7: Astrometric orbital elements for  $\psi^1$  Dra Bb. For parameters derived from the MCMC analysis, we report their median values and their mean absolute deviation (in brackets).

### 5.2.2. Origin of the trend

In this Section, we investigate the nature of the long-term trend observed in the data. In particular, we ascertain whether  $\psi^1$  Dra A ( $a \approx 600$  AU,  $M_A \approx 1.38M_\odot$ ,  $P \approx 9.4 \times 10^4$  years; Toyota et al. 2009) is the source of the long-term trend.

To model the long-term trend, we first assume that the gravitational pull is provided by an external perturber ( $\psi^1$  Dra Bc) in a circular orbit. We fit the data by fixing the eccentricity of the perturber to zero and sampling periods between 4,000 days and 15,000 years. The top panel of Figure 17 shows the best-fit for the mass of the perturber at each period sampled. The goodness of the fit (as measured by the RMS of the residuals) is shown in the bottom panel. Beyond approximately  $10^4$  days, the RMS is flat and the period and mass of the perturber are degenerate. We note that component A cannot be the source of the long-term trend, given the minimum mass required for A at

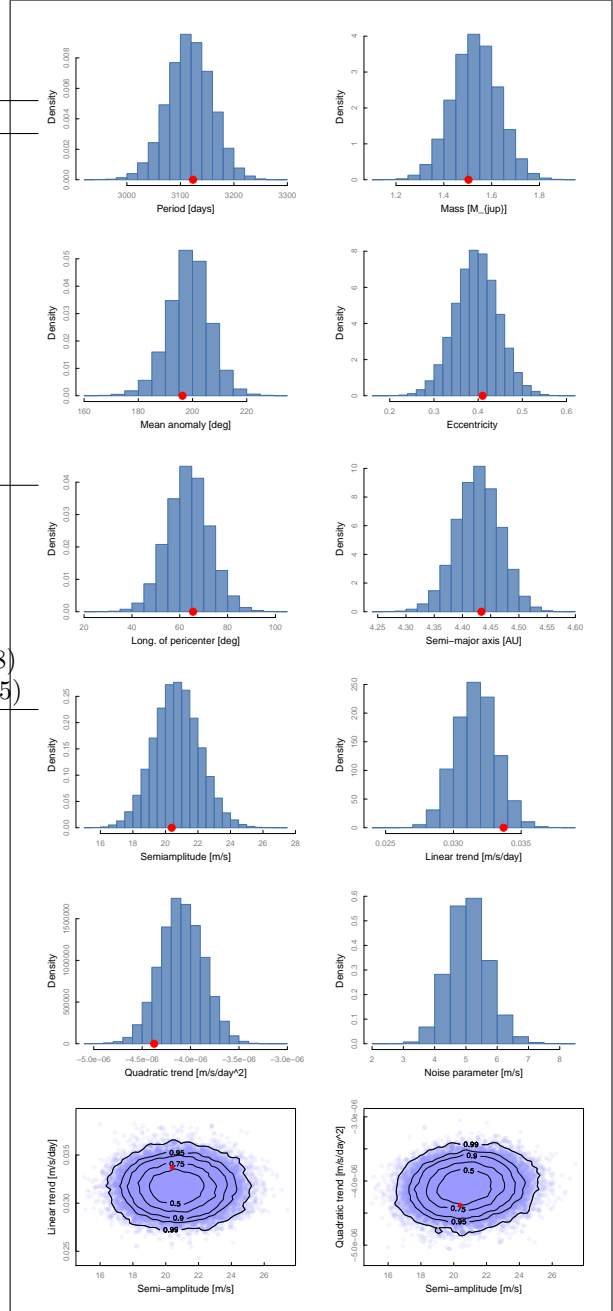


Fig. 15.— Marginal distributions of the orbital elements for the 1-planet model, as computed by the Markov-Chain Monte Carlo algorithm. The red dot marks the value of the best-fit solution. The bottom row shows a contour plot of the planet semi-amplitude  $K$  versus the linear and quadratic trend parameters.

the observed binary separation.

If we relax the assumption of a circular orbit for the external perturber, then the predicted mass of the perturber at each orbital period will be smaller at higher eccentricities (Figure 18). This is because at higher eccentricities and fixed periods, the curvature of the RV signal will be provided at the pericenter swing of the perturber. Therefore, the mass of the outer companion is determined by the pericenter distance ( $q = a(1 - e)$ ; Figure 18, bottom panel), as expected. Again, component A is not close or massive enough to produce the observed curvature.

### 5.2.3. Stellar Activity Check

We examined the Ca II  $S_{HK}$  values determined from the spectra of  $\psi^1$  Dra B. The mean  $S_{HK}$  index for this star is  $0.167 \pm 0.0008$ , which is a typical value for a magnetically quiet star (e.g. the inactive star  $\tau$  Ceti has  $S_{HK} = 0.167 \pm 0.0013$  measured from our spectra). We find a linear correlation coefficient of 0.116 of the  $S_{HK}$  with the RV values. This translates to a probability of  $p \approx 18\%$  that the null-hypothesis of no correlation is correct. Very small values of  $p$  would indicate a correlation between the two quantities, but they are not strongly correlated.

Figure 19 shows the result of a period search in the  $S_{HK}$  data. No strong peaks and thus significant periodicities are detected. We also note that there is virtually no power at the orbital period of planet b ( $P = 3117 \pm 42$  days, indicated as vertical dashed line in the figure). This indicates that the RV variations of  $\psi^1$  Dra B are not caused by stellar activity. There is, however, some moderate power at periods exceeding our time baseline. This can be due to a low-level trend in magnetic activity of the star, possibly caused by a very long activity cycle.

### 5.2.4. Dynamical Stability Analysis

A number of recent studies have highlighted the value of examining the dynamical behavior of candidate planetary systems as a critical part of the planet discovery process (e.g. Horner et al. 2012a,b; Robertson et al. 2012a,b; Wittenmyer et al. 2012a, 2014a). We therefore chose to carry out a detailed dynamical study of the stability of the proposed  $\psi^1$  Dra B system, as a function of the

orbit of the relatively unconstrained outer body.

As in our earlier work, we carried out a total of 126075 individual simulations of the  $\psi^1$  Dra B planetary system, following the evolution of the two candidate planets for a period of 100 Myr using the *Hybrid* integration package within the n-body dynamics program MERCURY (Chambers, 1999). For these simulations, we have ignored the binary companion  $\psi^1$  Dra A – with a projected orbital separation of  $\sim 600$  AU, it is expected to have a negligible effect on the dynamics of the two planets considered here. In the case that one of the planets collided with the other, or was either flung into the central body or ejected from the system, the time at which that event occurred within the simulation was recorded, and the simulation was then terminated. This allowed us to create a map of the dynamical stability of the  $\psi^1$  Dra B system as a function of the initial semi-major axis and eccentricity of the outermost planet, as can be seen in Figure 20.

In each of our 126,075 simulations, we used the same initial conditions for the orbit of the innermost planet, as given in Table 6. For  $\psi^1$  Dra B c, we systematically varied the semi-major axis, eccentricity, argument of periastron ( $\omega$ ) and mean anomaly ( $M$ ) to create a grid of  $41 \times 41 \times 15 \times 5$  possible orbital solutions for that planet. In the case of the planet’s semi-major axis,  $\omega$ , and mean anomaly, we sampled the full  $\pm 3\sigma$  range around the nominal best fit values for each parameter. The parameters we used for planet c were as follows:  $a = 16.2 \pm 3.7$  AU;  $\omega = 299 \pm 10$  degrees, and mean anomaly  $M = 299 \pm 10$  degrees. For the eccentricity, we sampled 41 equally spaced values ranging between 0.0 and 0.5. This allowed us to investigate in some depth the influence that the eccentricity of the planet’s orbit will have on the system’s stability.

The results of our simulations can be seen in Figure 20. At each of the a-e locations in that figure, the lifetime given is the mean of 75 individual runs, sampling the full  $\omega - M$  parameter space. Most readily apparent in Figure 20 is that the nominal best-fit orbit is located in a broad region of orbital stability. Indeed, all solutions within  $\pm 1\sigma$  of the best-fit semi-major axis are dynamically stable, unless the initial orbital eccentricity is in excess of 0.2. This is not surprising: the relatively sharp delineation between stable and

unstable orbits that can be seen curving upwards from an origin at ( $a \sim 9, e \sim 0$ ) is a line of almost constant periastron distance, and separates those orbits on which the planets cannot experience close encounters from those on which they can (and do). Following Chambers et al. (1996), we can determine the mutual Hill radius of the two companions at various semi-major axes (using their equation 1). Doing this, we note that when  $\psi^1$  Dra B c is located at  $a = 9$  AU, the mutual Hill radius of the two companions is  $\sim 1.02$  AU, meaning that their orbits would be separated by less than 5 mutual Hill radii. More critically, however, this situation would allow the two companions to approach one another within two mutual Hill radii should a close encounter happen whilst  $\psi^1$  Dra B b (with its moderately large orbital eccentricity of 0.42) were close to apastron.

A few other noteworthy features can be readily observed in Figure 20. Interior to the broad area of stability lies a narrow island of stability at  $a \sim 7$  AU. Orbits in this region can be protected from destabilization by the influence of the mutual 2:1 mean-motion resonance between the two companions. Given an initial semi-major axis for  $\psi^1$  Dra B b of 4.31 AU, a perfect 2:1 commensurability between the orbits of the two planets would occur at  $a_c \sim 6.84$  AU, so long as the initial architecture of the system is appropriate, and the eccentricity of the orbit of  $\psi^1$  Dra B c is not too large. Such islands of resonant stability are not uncommon, and are thought to ensure the stability of several known exoplanetary systems (e.g. Wittenmyer et al. 2012b, Wittenmyer et al. 2014b).

Finally, a number of “bites” can be seen taken out of the broad region of stability – vertical strips of lower-than-average stability dotted at regular intervals through the whole range of semi-major axes examined (with the most prominent visible at  $a \sim 11$  AU). These represent locations where resonant interactions between the two companions act to destabilize, rather than stabilize, their orbits. These features serve as a reminder that even when two planets are well separated in their orbits around a given star, their orbits should still be checked for dynamical verisimilitude.

### 5.3. Direct Imaging

We observed both the A and B components of the  $\psi^1$  Draconis system separately with the Dif-

ferential Speckle Survey Instrument (DSSI) at the Gemini North telescope on 19 July 2014 UT. DSSI is a two-channel speckle camera described in Horch et al. (2009), which yields diffraction-limited information in two pass bands simultaneously. A 1000-frame sequence was recorded by each channel on each component. All frames were 60 ms exposures, and had format of  $256 \times 256$  pixels. The seeing for both observations was 0.65 arc seconds. The image scale is approximately 0.011 arcseconds per pixel for both cameras.

We reduced and analyzed the results as follows. We form the average autocorrelation and average triple correlation of the set of speckle frames, and from these we estimate both the magnitude and phase of the Fourier transform of the source. The former must be deconvolved by a point source observation in general; in the case of the data here, we constructed a point source matching the elevation and azimuth of the source by taking an observation of a point source at very high elevation and correcting it for the atmospheric dispersion expected for the elevation and azimuth of the science target. After the deconvolution, the magnitude and phase are assembled in the Fourier plane, low-pass filtered to suppress high-frequency noise, and inverse-transformed to arrive at a reconstructed (i.e. diffraction-limited) image of the target. More information about the reduction method with the current EMCCD cameras used with DSSI can be found in Horch et al. (2011).

With the reconstructed image in hand, we attempt to find companions by first examining the image. The images are shown in Figure 21. This yielded a strong stellar candidate at approximate separation of 0.16 arcseconds from the primary star for  $\psi^1$  Dra A, but no candidates for  $\psi^1$  Dra B.

We then also computed a detection limit curve for the image; that is, a curve showing the largest magnitude difference that could be detected as a function of separation from the central star in the image. To construct the curve, we choose a set of concentric annuli centered on the central star, and determine the statistics of the local maxima (peaks) occurring inside the annulus. If a peak in the annulus has a value of more than five times the sigma of all of the peaks above the average value of the peaks, we consider it to be a definitive detection of a stellar companion. Details of this

process for Gemini data can be found in e.g. Horch et al. (2012).

Figure 22 shows the detection limit curves for the four reconstructed images. The line in these figures is the 5-sigma detection limit. If a source is a formally above a 5-sigma detection, it would appear as a square data point lying below the curve. For  $\psi^1$  Dra B, there are no plausible sources. For  $\psi^1$  Dra A, we see a nearly 5-sigma detection of a second star at a separation of about 0.16 arcsec from the primary in the 880-nm image. In the 692-nm image, the same peak appears, but it is not as close to the 5-sigma line. Looking again at the two images, we see that these data correspond in both cases to the peak at pixel (114, 129). Since both images show the same peak in the same spot, we are very confident that this component is stellar in nature. In these images north is essentially up, and east is to the left, although there is a tilt of the celestial coordinates relative to pixel axes of about 5 degrees.

We next used our power spectrum fitting routine to determine the separation, position angle, and magnitude difference of the secondary. The results are summarized in Table 8, when deconvolving by the calculated point sources described above.

Since  $\psi^1$  Dra B is not resolved in our images, we also used it as the point source to deconvolve the images of  $\psi^1$  Dra A, and in doing the power spectrum fitting that way, we obtain the results summarized in Table 9.

The differences between these numbers and the above give an estimate for the internal precision of the measurement technique. In looking at the power spectra for each file, we also see clear fringes that match the location shown in the reconstructed image. This gives an additional layer of confidence that we have detected a real stellar companion.

filter (nm)	position angle (deg)	separation (arcsec)	magnitude difference (mag)
692	91.8	0.155	4.13
880	91.5	0.158	3.80

Table 8: Results of imaging for  $\psi^1$  Dra A, using generic point source deconvolution

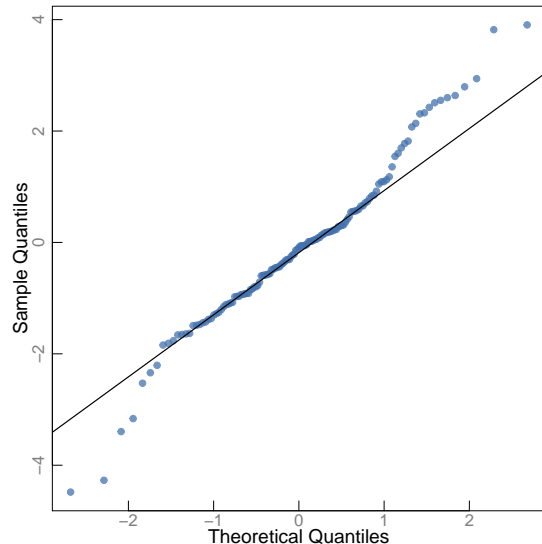


Fig. 16.— Quantile-quantile plot of the residuals from the 1-planet model. Perfectly normally distributed residuals would fall on the solid line.

filter (nm)	position angle (deg)	separation (arcsec)	magnitude difference (mag)
692	91.8	0.156	4.22
880	91.3	0.158	3.71

Table 9: Results of imaging for  $\psi^1$  Dra A, using  $\psi^1$  Dra B point source deconvolution.

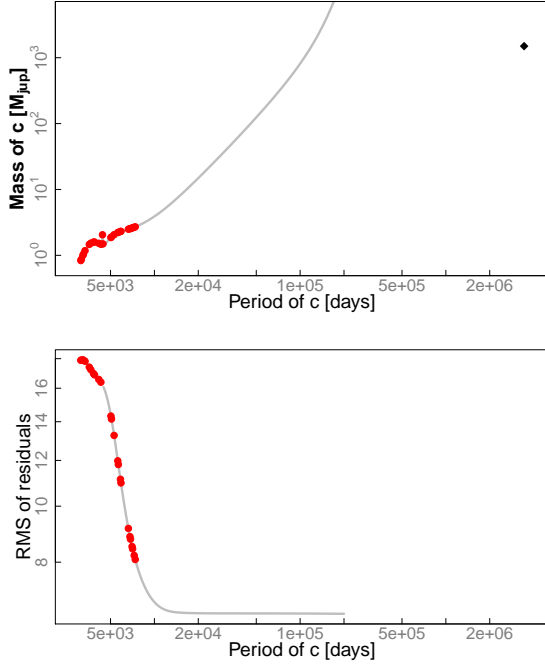


Fig. 17.— *Top*: Correlation between the period and the mass of an outer body in a circular orbit that best fits the trend in the RV data. The red points correspond to systems that were unstable over a  $10^6$  years period. The black diamond marks the semi-major axis and mass of component  $\psi^1$  Dra A from Toyota et al. (2009). *Bottom*: RMS of the residuals for the best-fit at each orbital period of the outer companion. At periods larger than  $\approx 10^4$  days, the marginal distributions of the period and mass of the outer companion are flat.

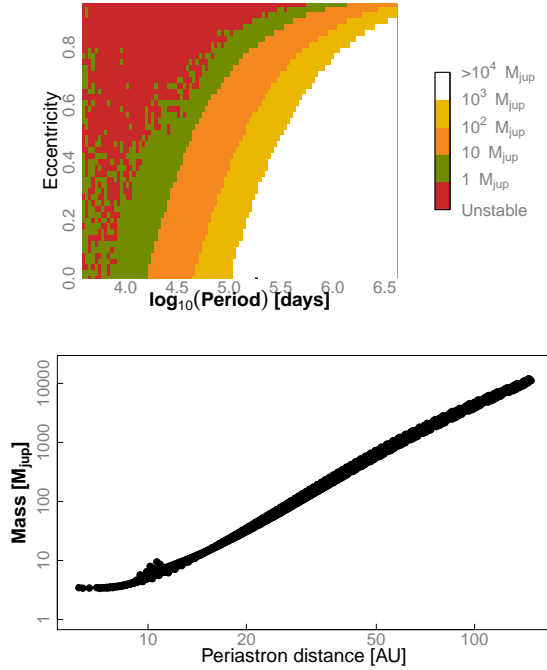


Fig. 18.— *Top*: Contours of best-fit masses for the outer perturber, computed over a grid of fixed periods and eccentricities. Systems unstable within  $10^5$  years are marked in red. *Bottom*: Relationship between the periastron distance and the mass of the outer perturber.

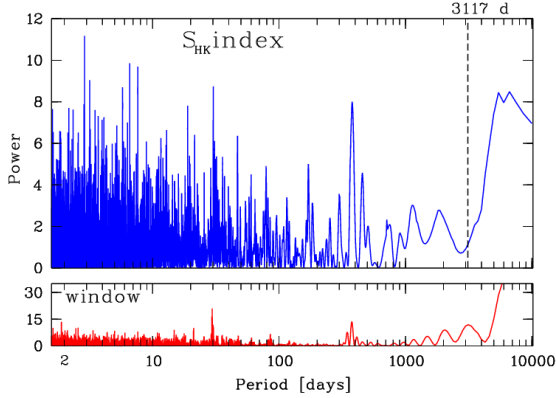


Fig. 19.— Lomb-Scargle periodogram of the Ca II  $S_{HK}$  index values of  $\psi^1$  Dra B (top) and the window function of our observations. The vertical dashed line indicates the orbital period of planet b. No power is detected at the planet’s period. There is moderate power at periods exceeding our time baseline ( $> 6000$  days). This could be due to a low-level long-term trend in the magnetic activity of this star.

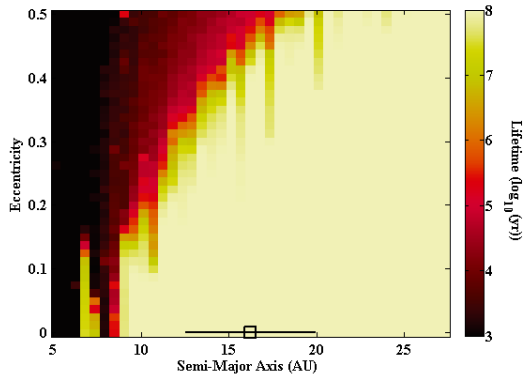


Fig. 20.— Dynamical stability map in semi-major axis and eccentricity space for the outer companion in the  $\psi^1$  Dra B system. Dark areas represent unstable regions (see text for details).

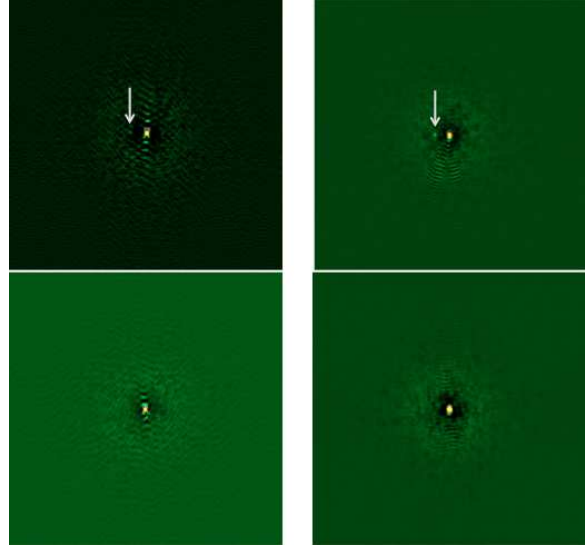


Fig. 21.— Reconstructed images of  $\psi^1$  Draconis A and B taken with the Differential Speckle Survey Instrument on the Gemini North telescope, 19 July 2014 UT. Each frame is  $2.8 \times 2.8$  arc seconds in size. Top left:  $\psi^1$  Draconis A at 692 nm. Top right:  $\psi^1$  Draconis A at 880 nm. Bottom left:  $\psi^1$  Draconis B at 692 nm. Bottom right:  $\psi^1$  Draconis B at 880 nm. A faint very red companion is visible to the left of the primary star in the A images; the separation is 0.16 arcsec.

## 5.4. Comparison of Elemental Abundances

### 5.4.1. Planet signatures in stellar abundances

An independent stellar parameter and detailed (multi-element) chemical composition analysis for both stars in the  $\psi^1$  Draconis system was carried out in order to search for chemical abundance anomalies that could be related to planet formation processes, as suggested by a number of recent studies. In their highly precise spectroscopic studies of Solar twin stars, Melendez et al. (2009) and Ramirez et al. (2009) have found the Sun to be slightly deficient in refractory elements, attributing this observation to the formation of rocky bodies in the Solar System. They suggest that these objects captured the refractory elements that would have otherwise ended up in the Sun. In related work, Ramirez et al. (2011) and Tucci Maia et al. (2014) have found that the two Solar-analog components of the 16 Cygni binary system have slightly different overall metal-

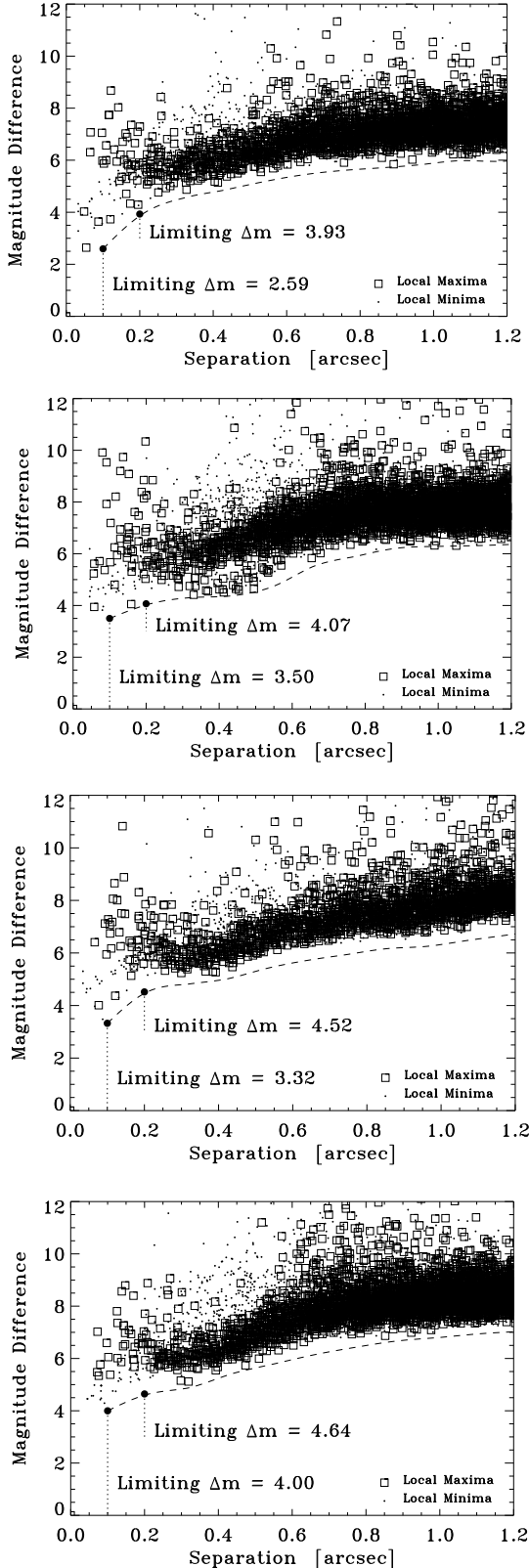


Fig. 22.— Detection limit curves as a function of separation for (a)  $\psi^1$  Dra A at 692 nm, (b)  $\psi^1$  Dra A at 880 nm, (c)  $\psi^1$  Dra B at 692 nm, and (d)  $\psi^1$  Dra B at 880 nm. These data are derived from the speckle image reconstructions as

licities and have attributed this effect to the formation of the gas giant planet that orbits 16 Cygni B (Cochran et al. 1997).

The rocky planet formation hypothesis for the refractory element depletion seen in the Sun has been challenged by Gonzalez-Hernandez et al. (2010, 2013) while Schuler et al. (2011) have found no chemical abundance differences for the 16 Cygni stars. Thus, further investigation of other relevant stellar systems could shed light on this problem. The  $\psi^1$  Draconis system is an interesting target in this context. Although not similar to the Sun, these stars are similar to each other, which is favorable to high-precision relative chemical composition analysis. Our  $\psi^1$  Dra A spectrum is contaminated by the light from the stellar companion at the 1% level.

#### 5.4.2. Atmospheric parameter determination

We acquired very high signal-to-noise ratio spectra of the  $\psi^1$  Draconis stars with the Tull spectrograph on the 2.7m Telescope at McDonald Observatory on 21 April 2014. At 6000 Å, these spectra have  $S/N \simeq 500$  per pixel and a spectral resolution  $R = 60\,000$ . These spectra are not part of the RV planet search data set; they were acquired specifically for the purpose of carrying out a detailed, strict differential atmospheric parameter and chemical abundance analysis. As described below, we analyzed  $\psi^1$  Dra A relative to  $\psi^1$  Dra B, but we also tested our differential calculations using a Solar spectrum as reference. The latter was taken from a previous observing run (18 December 2013) in which reflected sunlight from the asteroid Vesta was used to collect a high signal-to-noise ratio ( $S/N \simeq 350$  at 6000 Å) Solar spectrum with the same instrument/telescope and identical configuration.

Equivalent widths of 73 Fe I lines and 18 Fe II lines were measured by fitting Gaussian profiles to the observed spectral lines in the  $\psi^1$  Draconis stars' and Solar spectra using the `splot` task in IRAF. The linelist and atomic parameters adopted are those by Ramirez et al. (2013). The uncertainty of the adopted  $\log g f$  values and whether those were taken from laboratory measurements or calibrated using reference spectra (i.e., “astrophysical” values) are irrelevant in the strict differential approach implemented here. As mentioned above, the  $\psi^1$  Dra A spectrum is contaminated at



the 1 % level by its stellar companion. We noticed this minor contamination in our spectra and attempted to remove it in our equivalent width measurements by using the “deblend” feature of `splot` whenever possible or by excluding sections of line wings in the line profile fits. Nevertheless, we expect the equivalent widths measured for  $\psi^1$  Dra A to be less precise than those of  $\psi^1$  Dra B, not only due to the spectral contamination, but also because of its somewhat faster projected rotational velocity.

The equivalent widths of each of the  $\psi^1$  Draconis stars and the Sun were employed to calculate iron abundances using the `abfind` driver of the MOOG spectrum synthesis code, adopting Kurucz’s `odfnew` grid of model atmospheres interpolated linearly to the assumed atmospheric parameters of each star. Then, on a line-by-line basis, differential iron abundances relative to the Sun were computed for the  $\psi^1$  Draconis stars. The stellar parameters of the  $\psi^1$  Draconis stars were modified iteratively until correlations of the iron abundance with excitation potential and reduced equivalent width disappeared and until the mean abundance of iron derived from Fe I and Fe II lines separately agreed. This procedure is standard in stellar spectroscopy (cf Section 3.3) and it is sometimes referred to as the excitation/ionization equilibrium method of stellar parameter determination. To be more specific, hereafter we refer to this technique as the “iron line only” method. The particular implementation used here, including the error analysis, is described in detail in Ramirez et al. (2014; Sect. 3.1 and references therein).

The atmospheric parameters of the  $\psi^1$  Draconis stars, derived as described above, are given in the first two rows of Table 10. The errors listed in that table are formal, i.e., they represent the precision with which we are able to find a self-consistent solution for the parameters, but do not take into account possible systematic errors. The  $\psi^1$  Draconis

stars are both significantly warmer than the Sun. Thus, we expect the analysis using the Solar spectrum as reference to be affected by systematic errors in a non-negligible way. Since we are interested in the relative elemental abundances of the two  $\psi^1$  Draconis stars, we could attempt to reduce these formal errors, and also minimize the potential systematics, by analyzing  $\psi^1$  Dra A using  $\psi^1$  Dra B as the reference star. Adopting the parameters derived for  $\psi^1$  Dra B using the Sun as reference (row 2 in Table 10), we computed the parameters of  $\psi^1$  Dra A given in row 3 of Table 10. Note that the formal errors reduced, but the average values of the parameters were not significantly affected. This demonstrates that, when using the Sun as reference, systematic errors are introducing line-to-line scatter to the iron abundances of the  $\psi^1$  Draconis stars.

In the last step we implicitly assumed that the parameters of  $\psi^1$  Dra B derived using the Sun as reference are reliable. We tested this assumption by computing those parameters using independent techniques. For  $T_{\text{eff}}$ , we employed the effective temperature – color calibrations by Casagrande et al. (2010). For  $\log g$ , we used the stars’ trigonometric parallaxes as given in the *Hipparcos* catalog along with the Yonsei-Yale theoretical isochrone grid. Details on these techniques and the implementation used here are also provided in Ramirez et al. (2014; Sects. 5.1 and 5.3 and references therein).

Using the  $[\text{Fe}/\text{H}]$  values from Table 10, the Casagrande et al. (2010)  $T_{\text{eff}}$  calibrations for the  $(B-V)$ ,  $(b-y)$ , and  $(B_T-V_T)$  colors provide mean values of  $6519 \pm 20$  K for  $\psi^1$  Dra A and  $6194 \pm 21$  K for  $\psi^1$  Dra B. Both these values are in agreement within formal error with those computed from the iron lines only (i.e., with the parameters given in Table 10). Moreover, their difference is 325 K according to the  $T_{\text{eff}}$ -color calibrations and 333 K according to the iron line analysis. This test confirms that the  $T_{\text{eff}}$  adopted for  $\psi^1$  Dra B in the strict differential analysis for  $\psi^1$  Dra A is reliable.

The trigonometric  $\log g$  values were computed using the  $T_{\text{eff}}$  from the color calibrations, thus making them completely independent of the iron line only analysis. We calculated  $\log g = 4.02 \pm 0.02$  for  $\psi^1$  Dra A and  $\log g = 4.32 \pm 0.02$  for  $\psi^1$  Dra B. The spectroscopic (iron line only)  $\log g$  of  $\psi^1$  Dra A appears slightly low, yet it is still in

Table 10: Atmospheric Parameters of the  $\psi^1$  Draconis Stars

Star	$T_{\text{eff}}$	$\log g$	$[\text{Fe}/\text{H}]^3$
A	$6546 \pm 56$	$3.90 \pm 0.14$	$-0.10 \pm 0.04$ ( $\pm 0.07$ )
B	$6213 \pm 20$	$4.35 \pm 0.05$	$+0.00 \pm 0.01$ ( $\pm 0.04$ )
A	$6544 \pm 42$	$3.90 \pm 0.11$	$-0.10 \pm 0.03$ ( $\pm 0.05$ )

marginal agreement with the trigonometric value within formal error. However, for  $\psi^1$  Dra B, the agreement is excellent, which also suggests that the  $\log g$  adopted for  $\psi^1$  Dra B in the strict differential analysis of  $\psi^1$  Dra A is reliable.

As part of this calculation, we also computed age probability distributions for these stars using the same Yonsei-Yale isochrone set. We found most-probable ages of 2.3 and 2.5 Gyr for  $\psi^1$  Dra A and  $\psi^1$  Dra B, respectively, both with precision errors of order 0.3 Gyr. The details of this calculation are explained in Ramirez et al. (2014, their Sect. 4.5). Note in particular that the errors do not include systematic uncertainties from the stellar models. The ages quoted above are somewhat younger than that given in Table 1 for  $\psi^1$  Dra B (3.3 Gyr), but note that the latter has a much larger error bar due to the less precise stellar parameters employed. In fact, this age is consistent within error with the values listed here. In any case, the ages determined with the parameters measured as described in this section, which are based on higher quality spectra, lead to consistent ages for  $\psi^1$  Dra A and  $\psi^1$  Dra B, as expected for a binary system.

#### 5.4.3. Multi-element abundance analysis

Equivalent widths of spectral lines due to species other than iron were measured to compute differential abundances of 20 chemical elements in the  $\psi^1$  Draconis stars. The linelist and adopted atomic data, including hyperfine structure parameters when available, are from Ramirez et al. (2009, 2011). Oxygen abundances were inferred using the O I triplet lines at 777 nm, corrected for non-LTE effects using the grid by Ramirez et al. (2007).

The relative elemental abundances we measured are plotted in Figure 23 as a function of the elements' 50 % condensation temperatures, as computed by Lodders et al. (2003) for a Solar composition gas. Note that this “A–B” difference in chemical abundances was obtained when  $\psi^1$  Dra A was directly analyzed with respect to  $\psi^1$  Dra B in a strict line-by-line differential manner. The error bars are significantly smaller compared to the case in which the elemental abundances are first determined with respect to the Sun and then subtracted. This is a consequence of reducing the systematic errors of the analysis by avoiding a ref-

erence that is very dissimilar to either one of the  $\psi^1$  Draconis stars.

Figure 23 shows that  $\psi^1$  Dra A is metal-poor relative to  $\psi^1$  Dra B. On average, the metallicity difference is  $-0.09 \pm 0.04$  dex. We do not detect a statistically significant correlation with the condensation temperature, but this is likely due to the relatively large errors in the abundance differences. In the Meléndez, Ramírez, et al. works the precision of relative abundances is of order 0.01 dex. In our case those errors are about 0.04 dex instead. Thus, we cannot rule out possible trends based on our data.

One may be tempted to attribute the elemental abundance discrepancy shown in Figure 23 to uncertain stellar parameters. The derived chemical abundances are most affected by the adopted  $T_{\text{eff}}$  values, and we have shown above that those of  $\psi^1$  Dra B are reliable. Thus, we can explore this potential systematic error by simply calculating the relative abundances for different  $T_{\text{eff}}$  values for  $\psi^1$  Dra A and keeping everything else constant. Increasing the  $T_{\text{eff}}$  of  $\psi^1$  Dra A by 200 K would make the average elemental abundance difference nearly zero, but only for refractory elements ( $T_{\text{cond}} \gtrsim 1000$  K). The abundances of C and O in this case would differ by about  $-0.2$  dex. On the other hand, decreasing the  $T_{\text{eff}}$  of  $\psi^1$  Dra A by 200 K would make the C and O abundances difference nearly zero, but then the refractories would differ by about  $-0.2$  dex. In both cases, we note that the element-to-element scatter as well as the line-to-line relative abundance scatter for individual elements increase relative to the case when our derived  $T_{\text{eff}}$  value is adopted instead. In other words, the elemental abundance differences are more internally consistent for our derived parameters, suggesting that the hotter or cooler temperatures of  $\psi^1$  Dra A are not realistic (within our modeling assumptions, of course). Thus, it is not possible to reconcile the chemical abundance difference between  $\psi^1$  Dra A and B by assuming that the  $T_{\text{eff}}$  of the former is either underestimated or overestimated. The spectral contamination of  $\psi^1$  Dra A can not explain the observed abundance difference either. Since only 1 % of the flux is from the low-mass stellar companion, the equivalent widths and abundances derived could have been underestimated by 1 % at most. This corresponds to less than about 0.005 dex in  $[X/H]$ . We

are led to conclude that the offset seen in Figure 23 is real.

#### 5.4.4. Does $\psi^1$ Dra A have $\delta$ Scuti abundances?

The chemical composition of  $\delta$  Scuti stars may be peculiar. The prototype star of this class shows a severe enhancement, up to about 1.0 dex, in the abundances of elements with atomic number above 30 (Yushchenko et al. 2005). A very similar abundance pattern is observed in  $\rho$  Puppis, a very bright  $\delta$  Scuti star, as shown by Gopka et al. (2007). Note, however, that both  $\delta$  Scuti and  $\rho$  Puppis are about 500 K warmer than  $\psi^1$  Dra A.

A  $\delta$  Scuti star with known detailed chemical abundances which is more similar in stellar parameters to  $\psi^1$  Dra A is CP Boo (Galeev et al. 2012). This star is about 200 K cooler than  $\psi^1$  Dra A, and a bit more metal rich ( $[\text{Fe}/\text{H}]=+0.16$ ). The abundances measured by Galeev et al. also reveal enhancements of the heavy metals, but not as dramatic as in  $\delta$  Scuti and  $\rho$  Puppis. On average, the abundances of elements with atomic number above 30 are higher by about 0.3 dex. Such level of enhancement would be easily detected in our spectra. Figure 23 shows that at least the abundances of Zn ( $Z=30$ ,  $T_c=726\text{K}$ ), Y ( $Z=39$ ,  $T_c=1659\text{K}$ ), Zr ( $Z=40$ ,  $T_c=1741\text{K}$ ), and Ba ( $Z=56$ ,  $T_c=1455\text{K}$ ) are not enhanced in  $\psi^1$  Dra A relative to  $\psi^1$  Dra B. They are also not enhanced when the abundances are measured relative to the Solar abundances.

To provide further evidence for this finding, we measured the abundances of Nd ( $Z=60$ ,  $T_c=1594\text{K}$ ) and Eu ( $Z=63$ ,  $T_c=1347\text{K}$ ) using spectrum synthesis following the procedure described in Ramirez et al. (2011). For both of these species we found an A-B difference of  $-0.10 \pm 0.06$  dex. In other words, the Nd and Eu abundances of  $\psi^1$  Dra A relative to  $\psi^1$  Dra B fit perfectly the pattern seen in Figure 23. In particular, they are also not enhanced in the former. An enhancement of 1.0 dex, as in  $\delta$  Scuti or  $\rho$  Puppis, or even the mild enhancement of 0.3 dex seen in CP Boo would have been trivial to detect in our analysis. In fact, in that case some points would be found out of the chart in Figure 23.

Although the abundance pattern of  $\psi^1$  Dra A does not look like that of some prototypical  $\delta$  Scuti stars, it should be noted that these peculiarities may not correlate perfectly with the stars' pulsa-

tion characteristics. In fact, Fossati et al. (2008) argue that  $\delta$  Scuti stars have abundance patterns that are indistinguishable from a sample of normal A- and F-type stars. Thus, the non-enhancement of heavy metal abundances that we find for  $\psi^1$  Dra A does not necessarily rule it out as a candidate for a star of the  $\delta$  Scuti class.

#### 5.4.5. Possible interpretations

In the 16 Cygni system, the secondary hosts a gas giant planet whereas the primary has not yet shown evidence of sub-stellar mass companions. Ramirez et al. (2011) found that 16 Cyg B is slightly metal-poor relative to 16 Cyg A and explained this observation as a signature of planet formation. Briefly, they suggested that the missing metals of 16 Cyg B are currently located inside its planet. Considering that hypothesis, possible explanations for our results regarding the  $\psi^1$  Draconis system include:

1. The 16 Cygni planet signature hypothesis is incorrect because in  $\psi^1$  Draconis, the secondary, which is a gas giant planet host, is actually more metal-rich than the primary, which does not show evidence of hosting planets in our RV data. Metals should have been taken away from the planet-host star  $\psi^1$  Dra B and that star should be metal-poor relative to  $\psi^1$  Dra A, which is the opposite of what we observe. In this case, the cause of the observed abundance differences seen in both 16 Cygni and in  $\psi^1$  Draconis remains unknown.
2. Planet-like material and perhaps even fully-formed planets were once present in orbit around  $\psi^1$  Dra A, with a total mass greater than that of  $\psi^1$  Dra B's planet or planets combined. However, the stellar companion  $\psi^1$  Dra C made the planetary environment unstable, ejecting all of the planet material away from  $\psi^1$  Dra A. In this scenario, the outer layers of  $\psi^1$  Dra A would have accreted metal-poor gas during the planet-formation stage. The metals missing from  $\psi^1$  Dra A would have been locked-up in the material that was ejected later. The late ejection of that material is required to explain our non-detection of planets around  $\psi^1$  Dra A.

Since  $\psi^1$  Dra B has a planet (or two), its atmosphere is also depleted in metals relative to the initial metallicity of the system, but the metal depletion suffered by  $\psi^1$  Dra A was greater. The latter would be easily explained by a larger total mass of planet-like material, but it could also be in part due to the thinner convective envelope of this warmer star, which did not dilute the chemical signature as much as  $\psi^1$  Dra B.

3.  $\psi^1$  Dra A never formed planets due to the influence of its low-mass stellar companion. On the other hand,  $\psi^1$  Dra B formed much more planet-like material than seen today in the planet or planets that we have detected. A fraction of this material, that which is not in the planet(s) detected by us, was accreted into the star at a later stage, increasing the metallicity of its atmosphere. The amount of planet material accreted that is necessary to explain our observations had to have been larger than the total mass of the planet or planets detected. This is because the formation of those planets imply that metals were already taken away from the star and this needs to be first compensated in order to result in a stellar atmosphere that is more metal rich than the birth cloud of the system. In this scenario, the metallicity of  $\psi^1$  Dra A is that of the gas cloud from which both stars formed whereas  $\psi^1$  Dra B's atmosphere became metal-rich at a later stage.
4. Planets did also form around  $\psi^1$  Dra A, but we did not detect them because the  $\delta$  Scuti pulsations and spectral contamination from  $\psi^1$  Dra C lead to the observed large RV-jitter that prevents the detection of the RV-signature of any planet around this star. Another way the planets could avoid detection by the RV method is if the angle between the planetary orbital planes and the sky is small.

Finally, we note that the potential post-main-sequence nature of  $\psi^1$  Dra A could have allowed dredge-up to occur in that star. However, this mechanism is expected to enhance the metallicity of the stellar convection zone and photosphere while the effect that we observe is that of a depletion of metals in  $\psi^1$  Dra A. Thus, dredge-up can

also be ruled out as a possibility to explain the abundance offset seen in Figure 23.

## 6. Two Cold Jupiter “False Alarms” Related to Stellar Activity

### 6.1. HD 10086

We have obtained 84 RV measurements of HD 10086 over approximately 16 years, as listed in Table 11. The RVs have an RMS of  $13.1 \text{ m s}^{-1}$  with a mean uncertainty of  $6.3 \text{ m s}^{-1}$ , indicating the potential presence of a periodic signal. The periodogram of the velocities (Figure 24) shows a broad and significant peak centered at 2800 days. This signal may be modeled as a circular Keplerian orbit with period 2800 days and a semi-amplitude  $K = 11 \text{ m s}^{-1}$ , which would correspond to a planet with a minimum mass  $M \sin i = 0.74 M_{\text{Jup}}$  at  $a = 3.9 \text{ AU}$ . Incidentally, HD 10086 was also included in the Lick Observatory RV survey (Fischer et al. 2014). The 40 Lick RVs have an RMS of  $18.6 \text{ m s}^{-1}$  and a mean uncertainty of  $3.6 \text{ m s}^{-1}$ . This independently confirms the apparent RV variability of this star.

	BJD	dRV ( $\text{m s}^{-1}$ )	Uncertainty ( $\text{m s}^{-1}$ )	$S_{HK}$	Uncertainty
1	2451152.7300	7.0	7.2	0.312	0.020
2	2451213.6509	-0.8	5.4	0.302	0.018
3	2451240.6034	37.4	10.9	0.299	0.017
4	2451452.8818	38.6	6.0	0.335	0.020
5	2451503.7088	21.5	7.1	0.327	0.021
6	2451530.7712	4.9	6.2	0.290	0.019
7	2451558.6106	20.5	6.6	0.304	0.020
8	2451775.9029	-2.8	5.7	0.273	0.020
9	...	...	...	...	...

Table 11: Differential radial velocity and Ca H&K observations for HD 10086 (sample).

However, in our analysis of stellar activity indicators for HD 10086, we see a similar 2800-d peak in the periodogram of the  $S_{HK}$  Ca H&K index, suggesting the RV modulation may reflect a stellar activity cycle rather than a giant planet. Considering RV as a function of  $S_{HK}$  (Figure 25, top panel) confirms this hypothesis. The RVs of HD 10086 are very strongly correlated with  $S_{HK}$ ; a Pearson correlation test yields a correlation coefficient  $r = 0.66$  which, for a sample size  $N = 84$  indicates a probability of  $P < 10^{-12}$  that we would

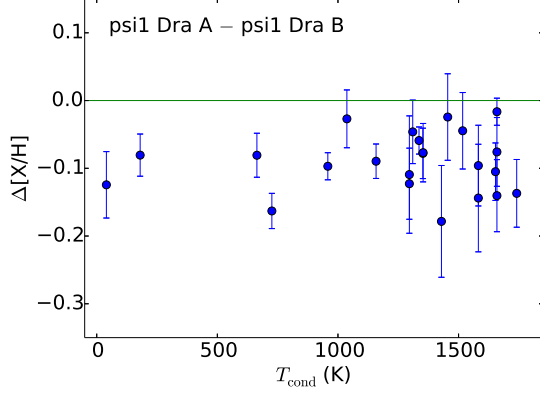


Fig. 23.— Elemental abundance difference between  $\psi^1$  Dra A and  $\psi^1$  Dra B as a function of the elements' condensation temperatures.

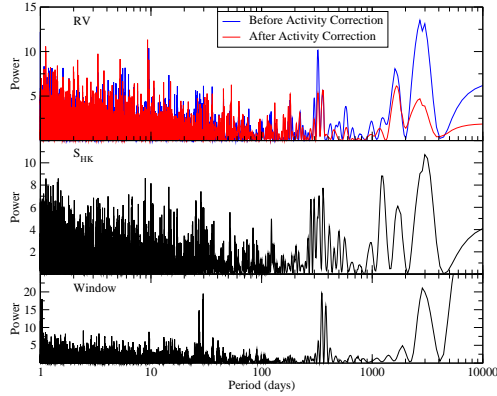


Fig. 24.— Generalized Lomb-Scargle periodograms of our RV data for HD 10086 before (blue) and after (red) correcting for stellar activity, along with the corresponding periodogram of  $S_{HK}$ .

observe such a correlation if RV and activity were uncorrelated.

Given the tight correlation between RV and Ca H&K emission for this star, we attempted to perform a simple stellar activity correction by fitting and removing a linear least squares model for RV versus  $S_{HK}$ . We find a linear fit of  $v_r = -120(15) + 420(50) \times S_{HK}$ . Upon subtracting this model from the RVs, we see from the activity-corrected periodogram that the 2800-day signal is almost completely eliminated, providing final confirmation that this signal is caused by Doppler shifts associated with a 7.7-year activity cycle. We show both RV and  $S_{HK}$  folded to the period of this cycle in Figure 25. We see no statistically significant additional signals in RV, and conclude we have not discovered any exoplanets around this star to date.

## 6.2. $\beta$ Virginis

We have observed  $\beta$  Virginis (hereafter  $\beta$  Vir) for approximately 16 years, obtaining a total of 311 RV measurements, as listed in Table 12. These velocities have an RMS of  $9.0 \text{ m s}^{-1}$  with a mean uncertainty of just  $3.7 \text{ m s}^{-1}$ . In Figure 26, we show the Lomb-Scargle periodogram of the RVs, which includes a broad, highly significant peak at approximately 2000 days. The best Keplerian model to the data produces an eccentric ( $e = 0.26$ ) orbit with  $P = 2040$  days and  $K = 9 \text{ m s}^{-1}$ .

	BJD	dRV ( $\text{m s}^{-1}$ )	Uncertainty ( $\text{m s}^{-1}$ )	$S_{HK}$	Uncertainty
1	2451009.6241	10.9	2.4	0.158	0.014
2	2451153.9622	0.7	6.0	0.164	0.020
3	2451213.0360	-4.4	2.5	0.159	0.020
4	2451241.8748	-11.3	3.2	0.176	0.020
5	2451274.7687	3.1	4.2	0.179	0.019
6	2451326.7453	1.6	3.1	0.168	0.017
7	2451358.6645	8.2	2.0	0.162	0.016
8	2451504.0169	2.0	2.2	0.166	0.023
9	...	...	...	...	...

Table 12: Differential radial velocity and Ca H&K observations for  $\beta$  Virginis (sample).

If the RV modulation is indeed produced by an exoplanet, this Keplerian model corresponds to a gas giant orbiting at  $a = 3.5 \text{ AU}$  with minimum mass of  $M \sin i = 0.65 M_{\text{Jup}}$ . As with HD

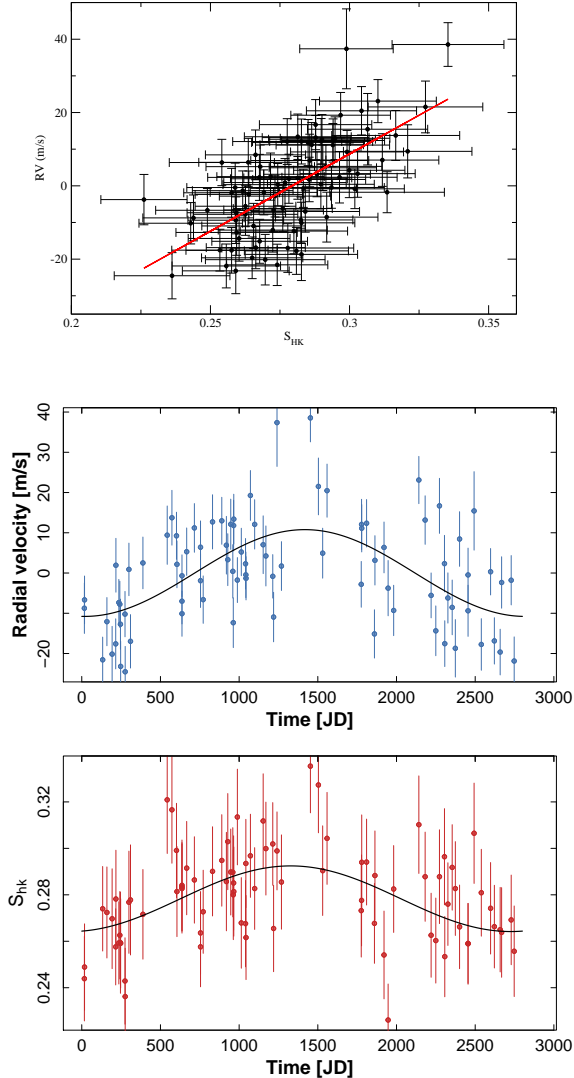


Fig. 25.— *Top Panel*: RV for HD 10086 as a function of  $S_{HK}$  at the time of each observation. The linear least-squares fit to the relation is given as a solid red line. *Middle and Bottom Panels*: RV and  $S_{HK}$ , respectively, folded to the 2800-day period of the stellar activity cycle. Sinusoidal models to each data set are shown as solid black curves.

10086, though, the Ca H&K emission of  $\beta$  Vir suggests the observed signal is not associated with a planet. We include the periodogram of  $S_{HK}$  in Figure 26, which also includes a very broad peak between 1000 and 2500 days. RV as a function of  $S_{HK}$  (Figure 27) again shows a highly significant correlation; we compute a Pearson correlation coefficient  $r = 0.39$  and a  $P$ -value of  $2 \times 10^{-12}$ . We therefore suspect the periodicity observed for  $\beta$  Vir is also a stellar activity cycle which mimics a Doppler shift such as would be expected for a Jupiter analog planet.

A number of features of our data set for  $\beta$  Vir prevent the application of a simple stellar activity correction analogous to the one we performed for HD 10086. First, the weaker calcium emission (mean  $S_{HK} = 0.17$ , versus 0.28 for HD 10086) leads to lower signal to noise in the Ca H&K measurements. Furthermore, our RVs show significant short-term scatter ( $5.1 \text{ m s}^{-1}$  over the 2013 observing season) and possibly a long-term linear acceleration in addition to the activity-induced periodicity. Finally, the “eccentricity” of the RV signal created by the activity cycle suggests the activity signal may be non-sinusoidal, and the RV-activity relationship may therefore not be linear. These factors make it especially difficult to fit and subtract a simple activity-RV dependence, and we therefore do not attempt a stellar activity correction for  $\beta$  Vir. The matching periodicities in RV and Ca H&K and the correlation between RV and  $S_{HK}$  lead us to conclude the observed signal is due to a stellar activity cycle, but the evaluation of any additional (possibly planetary) signals in the velocities must be postponed pending a more sophisticated stellar activity analysis, which is beyond the scope of this paper.

## 7. Discussion & Conclusion

We present two cases (HD 95782 and  $\psi^1$  Dra B) for gas giant planets at large orbital separations, in the Jupiter-analog range. Owing to the very long time baseline of over a decade or more, the RV discoveries of such planets are still relatively rare. Long-term precise RV surveys, like the McDonald Observatory planet search, still represent the current best capability to find these planets. These planets cannot be found by *Kepler*, nor *K2*, nor TESS (Ricker et al. 2015), due to the short time

span of monitoring, coupled with a very low transit probability of planets at 5 AU. And, despite that the best direct imaging instruments like *Gemini Planet Imager* (GPI, Macintosh et al. 2014) and *SPHERE* (Beuzit et al. 2008) reach the small inner working angles for nearby stars, the low luminosities of mature, old, Jupiters makes them virtually undetectable, even for these instruments. Discoveries of giant planet candidates like 51 Eri b (Macintosh et al. 2015) at very young ages of  $\sim 20$  Myrs and separations of  $a > 10$  AU will eventually allow us to find a complete picture for these type of planets in time and orbital separation space.

Another advantage of long-term RV surveys is the fact that we can use the RV data for all stars, where we do not detect a planet, to set tight constraints for the presence of these gas giants. These will allow to determine the occurrence rate of Jupiter analogs, and even of Solar System-type architectures with two gas giants.

The possibly crucial role of Jupiter, as well as of Saturn, for the formation of the terrestrial planets in our Solar System has been highlighted recently by Batygin & Laughlin (2015). These authors present a model, within the context of the “Grand Tack” model (Walsh et al. 2011), that explains why we do not have super-Earths in the inner Solar System, like the numerous *Kepler* systems. In their model, the migration of Jupiter (which is halted and reversed by Saturn’s dynamical evolution) depletes the interior protoplanetary disk, possibly driving all existing short-period super-Earths into the Sun. The low-mass terrestrial planets then subsequently formed in this depleted disk in the inner region of our Solar System. This model would therefore predict that planetary systems similar to ours can only form with at least two gas giants that end up at large separations after the early phase of migration has finished. The search for long-period gas giants therefore gains importance also in the search for Earth-like planets. The  $\psi^1$  Dra B planetary system could be an excellent candidate for a system with a planetary architecture very similar to our own, with two gas giants at large multi-AU separations, which possibly also helped the formation of lower mass rocky planets in the inner few AUs.

The other two stars, HD 10086 and  $\beta$  Vir, are stark reminders that stellar activity can mimic also the presence of Jupiter-analogs. Long-term

magnetic cycles can present themselves as slow RV modulations very similar to a Jupiter. Given that our Sun’s magnetic field cycle is comparable to Jupiter’s orbital period, we need to develop techniques that can correct for these effects and make planet detection possible, even in the presence of a stellar activity cycle. Our first approach to correlate the chromospheric emission in the Ca II H & K lines with the RV signal, works in a simple case like HD 10086. The need for a more sophisticated model is obvious in the case of  $\beta$  Vir. The relatively large RV amplitudes of the activity signal of several  $\text{m s}^{-1}$  is somewhat unexpected, especially for the relatively inactive stars  $\beta$  Vir. However, the SARG binary planet survey also found an activity cycle of the star HD 200466 A, that produces an RV signal with a semi-amplitude of  $\approx 20 \text{ m s}^{-1}$  (Carolo et al. 2014). It is thus clear that in our search for Jupiter-analogs, we need to expect activity-induced RV signals that can mimic even massive gas giants. Fortunately, all our spectra from the Tull instrument, contain the Ca II H & K lines and permit us an immediate test for possible activity cycles. The very long duration McDonald Observatory planet search at the 2.7 m HJST/Tull will therefore provide a unique data set for its entire sample of over 200 stars to find planetary systems similar to our own.

This work has been made possible through the National Science Foundation (Astrophysics grant AST-1313075) and various NASA grants over the years. We are grateful for their generous support. We also thank the McDonald Observatory Time Allocation committee for its continuing support of this program.

This research has made use of the SIMBAD database, operated at CDS, Strasbourg, France.

We would also like to thank all the observers who have helped gather data over the years for the 2.7 m radial velocity planet search program at McDonald Observatory, including Diane Paulson, Stuart I. Barnes, Candice Gray and Anita Cochran.

Finally, we would like to thank the anonymous referee: her/his comments helped to improve this paper.

*Facilities:* McDonald Observatory (Tull Coudé Spectrograph), Keck-I Observatory (HIRES)

## REFERENCES

- Andrae, R., Schulze-Hartung, T., & Melchior, P. 2010, arXiv:1012.3754
- Baliunas, S. L., Donahue, R. A., Soon, W. H., et al. 1995, *ApJ*, 438, 269
- Balona, L. A.; Daszyńska-Daszkiewicz, J. & Pamyatnykh, A. A. 2015, *MNRAS*, 452, 3073
- Batygin, K. & Laughlin, G. 2015, *PNAS*, accepted
- Bedell, M. et al. 2015, *A&A*, accepted
- Beuzit, J.-L. et al. 2008, *SPIE*, 7014, id. 701418, 12
- Borucki, W. J., Koch, D., Basri, G., et al. 2010, *Science*, 327, 977
- Carolo, E., Desidera, S., Gratton, R., et al. 2014, *A&A*, 567, 48
- Casagrande, L., Ramírez, I., Meléndez, J., Bessell, M., & Asplund, M. 2010, *A&A*, 512, 54
- Chambers, J. E., Wetherill, G. W., & Boss, A. P. 1996, *Icarus*, 119, 261
- Chambers, J. E. 1999, *MNRAS*, 304, 793
- Cochran, W. D., & Hatzes, A. P. 1993, in *ASP Conf. Ser. 36, Planets around Pulsars*, ed. J. A. Phillips, J. E. Thorsett, & S. R. Kulkarni (San Francisco, CA: ASP), 267
- Cochran, W. D., Hatzes, A. P., Butler, R. P., & Marcy, G. W. 1997, *ApJ*, 483, 457
- Endl, M., Kürster, M., Els, S. 2000, *A&A*, 362, 585
- ESA, 1997, *The Hipparcos and Tycho Catalogues*
- Fischer, D. A., Marcy, G. W., & Spronck, J. F. P. 2014, *ApJS*, 210, 5
- Ford, E. B. 2005, *AJ*, 129, 1706
- Ford, E. B. 2006, *ApJ*, 642, 505
- Fossati, L., Kolenberg, K., Reegen, P., & Weiss, W. 2008, *A&A*, 485, 257
- Fressin, F., Torres, G., Charbonneau, D., et al. 2013, *ApJ*, 766, 81
- Galeev, A. I., Ivanova, D. V., Shimansky, V. V., & Bikmaev, I. F. 2012, *Astronomy Reports*, 56, 850
- González Hernández, J. I., Delgado-Mena, E., Sousa, S. G., et al. 2013, *A&A*, 552, A6
- González Hernández, J. I., Israelian, G., Santos, N. C., et al. 2010, *ApJ*, 720, 1592
- Gopka, V., Yushchenko, A., Kim, C., et al. 2007, *The Seventh Pacific Rim Conference on Stellar Astrophysics*, 362, 249
- Gregory, P. C. 2011, *MNRAS*, 415, 2523
- Gullikson, K.; Endl, M.; Cochran, W. D.; MacQueen, P. J. 2015, *ApJ*, in press.
- Hatzes, A. P., Cochran, W. D., & Johns-Krull, C. M. 1997, *ApJ*, 478, 374
- Hatzes, A. P., Cochran, W. D., Endl, M., et al. 2003, *ApJ*, 599, 1383
- Horch, E. P., Veillette, D. R., Baena Gallé, R., Shah, S. C., O’Rielly, G. V., van Altena, W. F. 2009, *AJ*, 137, 5057
- Horch, E. P., Gomez, S., Sherry, W. H., Howell, S. B., Ciardi, D. R., Anderson, L., van Altena, W. F. R. 2011, *AJ*, 141, 45
- Horch, E. P., Howell, S. B., Everett, M. E., Ciardi, D. R. 2012, *AJ*, 144, 165
- Horner, J., & Jones, B. W. 2008, *International Journal of Astrobiology*, 7, 251
- Horner, J., Jones, B. W., & Chambers, J. 2010, *International Journal of Astrobiology*, 9, 1
- Horner, J., & Jones, B. W. 2010, *International Journal of Astrobiology*, 9, 273
- Horner, J., & Jones, B. W. 2012, *International Journal of Astrobiology*, 11, 147
- Horner, J., Wittenmyer, R. A., Hinse, T. C., & Tinney, C. G. 2012a, *MNRAS*, 425, 749
- Horner, J., Hinse, T. C., Wittenmyer, R. A., Marshall, J. P., & Tinney, C. G. 2012b, *MNRAS*, 427, 2812
- Howard, A. W.; Johnson, J. A.; Marcy, G. W. et al. 2010, *ApJ*, 721, 1467



- Howard, A. W., Marcy, G. W., Bryson, S. T., et al. 2012, *ApJS*, 201, 15
- Howard, A. W.; Marcy, G. W., Fischer, D. et al. 2014, *ApJ*, 794, 51
- Kim, Y., Demarque, P., Yi, S. K., & Alexander, D. R. 2002, *ApJS*, 143, 499
- Koen, C. 2006, *MNRAS*, 371, 1390
- Kürster, M., Schmitt, J.H.M.M., Cutispoto, G., & Dennerl, K. 1997, *A&A*, 320, 831
- Lodders, K. 2003, *ApJ*, 591, 1220
- Macintosh, B. et al. 2014, *SPIE*, 9148, id. 91480J, 14
- Macintosh, B. et al. 2015, *Science Express*, in press
- Marcy, G. W., Butler, R. P., Vogt, S. S., Fischer, D. A., Henry, G. W., Laughlin, G., Wright, J. T., & Johnson, J. A. 2005, *ApJ*, 619, 570
- Marmier, M., Ségransan, D., Udry, S. et al. 2013, *A&A*, 551, 90
- Meléndez, J., Asplund, M., Gustafsson, B., & Yong, D. 2009, *ApJ*, 704, L66
- Meschiari, S. Wolf, A. S., Rivera, E., Laughlin, G., Vogt, S., Butler, P. 2009, *PASP*, 121, 1016
- Moutou, C., Lo Curto, G., Mayor, M. et al. 2015, *A&A*, 576, 48
- Paulson, D. B., Saar, S. H., Cochran, W. D., & Hatzes, A. P. 2002, *AJ*, 124, 572
- Petigura, E. A., Howard, A. W., Marcy, G. W. 2013, *PNAS*, 110, 19273
- Ramírez, I., Allende Prieto, C., & Lambert, D. L. 2007, *A&A*, 465, 271
- Ramírez, I., Allende Prieto, C., & Lambert, D. L. 2013, *ApJ*, 764, 78
- Ramírez, I., Meléndez, J., & Asplund, M. 2009, *A&A*, 508, L17
- Ramírez, I., Meléndez, J., Bean, J., et al. 2014, *A&A*, 572, 48
- Ramírez, I., Meléndez, J., Cornejo, D., Roederer, I. U., & Fish, J. R. 2011, *ApJ*, 740, 76
- Raymond, S. N. 2006, *ApJ*, 643, 131
- Ricker, G. R., Winn, J. N., Vanderspek, R. et al. 2015, *JATIS*, 1, 014003
- Robertson, P., Endl, M., Cochran, W. D., et al. 2012a, *ApJ*, 749, 39
- Robertson, P., Horner, J., Wittenmyer, R. A., et al. 2012b, *ApJ*, 754, 50
- Schuler, S. C., Flateau, D., Cunha, K., et al. 2011, *ApJ*, 732, 55
- Soderblom, D. R., Duncan, D. K., & Johnson, D. R. H. 1991, *ApJ*, 375, 722
- Toyota, E., Itoh, Y., Ishiguma, S., Urakawa, S., Murata, D., Oasa, Y., Matsuyama, H., Funayama, H., Sato, B., Mukai, T. 2009, *PASJ*, 61, 19
- Tucci Maia, M., Meléndez, J., & Ramírez, I. 2014, *ApJ*, 790, L25
- Tull, R. G.; MacQueen, P. J.; Sneden, C.; Lambert, D. L. 1995, *PASP*, 107, 251
- Vogt, S.S., Allen, S.L., Bigelow, B.C., et al. 1994, *SPIE*, 2198, 362
- Walsh, K. J., Morbidelli, A., Raymond, S. N., O’Brien, D. P., Mandell, A. M. 2011, *Nature*, 475, 206
- Wittenmyer, R. A., Endl, M., Cochran, W. D., Hatzes, A. P., Walker, G. A. H., Yang, S. L. S., & Paulson, D. P. 2006, *AJ*, 132, 177
- Wittenmyer, R. A., Tinney, C. G., O’Toole, S. J., Jones, H. R. A., Butler, R. P., Carter, B. D., & Bailey, J. 2011a, *ApJ*, 727, 102
- Wittenmyer, R. A., Tinney, C. G., Butler, R. P., et al. 2011b, *ApJ*, 738, 81
- Wittenmyer, R. A., Horner, J., Tuomi, M., et al. 2012a, *ApJ*, 753, 169
- Wittenmyer, R. A., Horner, J., & Tinney, C. G. 2012b, *ApJ*, 761, 165
- Wittenmyer, R. A., Horner, J., Tinney, C. G., et al. 2014a, *ApJ*, 783, 103
- Wittenmyer, R. A., Tan, X., Lee, M. H., et al. 2014b, *ApJ*, 780, 140

Yi, S., Demarque, P., Kim, Y., et al. 2001, ApJS, 136, 417

Yushchenko, A.; Gopka, V.; Kim, C.; Musaev, F.; Kang, Y. W.; Kovtyukh, V.; Soubiran, C. 2005, MNRAS, 359, 865

Zechmeister, M., Kürster, M., Endl, M., et al. 2013, A&A, 552, A78

Zechmeister, M., Kürster, M. 2009, A&A, 496, 577

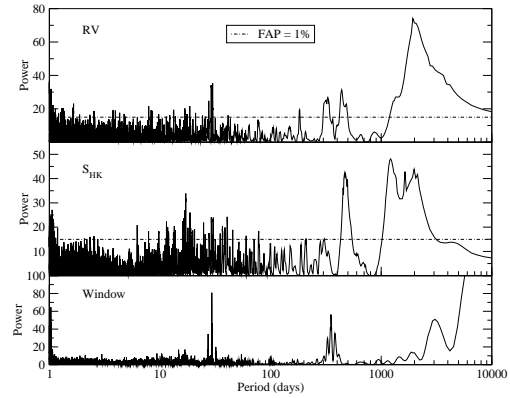


Fig. 26.— Generalized Lomb-Scargle periodograms of RV and  $S_{HK}$  for  $\beta$  Virginis. The threshold for a false alarm probability (FAP) of 1% is shown as a dash-dotted line.

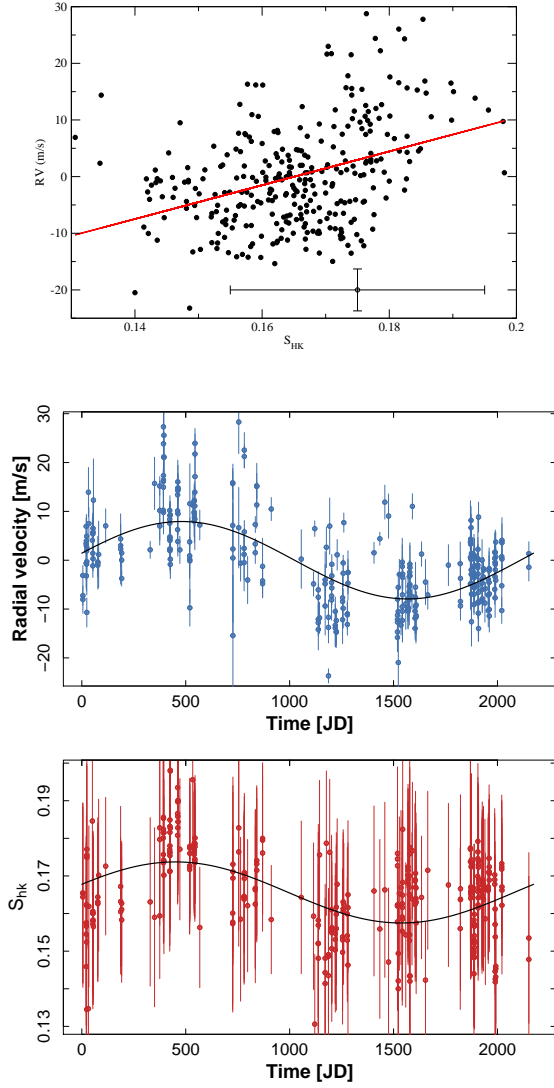


Fig. 27.— *Top Panel:* RV as a function of  $S_{HK}$  for  $\beta$  Virginis. The linear least squares fit to the data is shown as a solid red line. For the sake of visibility we do not show error bars on the individual points, but indicate the mean  $1\sigma$  uncertainty on each variable. *Middle and Bottom Panels:* RV and  $S_{HK}$ , respectively, folded to the 2200-day period of the stellar activity cycle. Sinusoidal models to each data set are shown as solid black curves.